博士論文

Time-ordered cone-beam CT image reconstruction

（　コーンビーム CT の時間並進的 4 次元画像再構成法　）

中 野　正 寛

Abstract

Four-dimensional (4D) cone-beam CT (CBCT) techniques have been used in clinical sites of image-guided radiotherapy (IGRT), especially in the treatment of lung tumors and other tumors accompanying respiratory motion. However, those techniques suppose periodic motion such as respiration, and there are few attempts using CBCT to visualize organs accompanying time-ordered non-periodic motion and deformation. The purpose of this study is to visualize time-ordered motion including gastrointestinal activities and motion of rectal gas and stools.

Reconstruction methods used in this study belong to two categories: Feldkamp-Davis-Kress (FDK) method and maximum *a posteriori* probability (MAP) method. The FDK method is the conventional one in CBCT reconstruction and widely used in medical region. One of the advantages in use of FDK method is that it works with a small computational effort. On the other hand, this method requires the projection data from more than 180-degree plus fan-angle to obtain the successful reconstruction images. Therefore, with the slow gantry rotation such as in the linear accelerator (LINAC), the FDK method accompanies the poor temporal resolution. The temporal resolution could be improved with the narrower projection angle range. Lacking the information due to the narrower projection angle range, however, the reconstructed image would be significantly degraded. A tradeoff of this approach between temporal resolution and image degradation was discussed in Chapter 2. In Chapter 3, a MAP reconstruction combined with initial image sets is proposed to resolve the problem with regard to narrower projection angle ranges. In addition to the total variation minimization approach and prior information constrained approach, both of which are previously proposed in the situation where the information is lacked, the constraint arising from time-ordered chain is newly introduced in order to improve temporal resolution. This new reconstruction method is named as Time-ordered chain graph model (TCGM) method. Two types of projection data sets are used for reconstruction test; clinical patients' pelvic region and virtually created digital phantom containing an air sphere moving 3 cm along longitudinal axis during one rotation of projection source around the phantom. Especially, the temporal resolution is analyzed with above digital phantom.

The present study demonstrates the feasibility of time-ordered 4D CBCT reconstruction dealing with time-ordered motion and deformation. Deformation of intestine and rectum, and motion of flatus and stool could be visualized by the presented method. The digital phantom results show that MAP method with TCGM improves its temporal resolution.

Abbreviation

ART : algebraic reconstruction technique

CBCT : cone-beam computed tomography

CC : cranio-caudal

CT : computed tomography

CTV : Clinical Target Volume

ECG : electrocardiogram

EPID : electric portal imaging device

FBP : Filtered Back Projection

FDK : Feldkamp, Davis and Kress

FOV : field-of-view

FPD : flat-panel detector

FWHM : Full Width of Half Maximum

GPU : graphical processing unit

GTV : Gross Tumor Volume

IGRT : image-guided radiotherapy

IM : Internal Margin

IMRT : intensity modulated radiotherapy

ITV : Internal Target Volume

MAP : Maximum *A Posteriori* possibility

MLC : Multi-Leaf Collimator

MLEM : Maximum Likelihood Expectation Maximization

PA : Posterior-to-Anterior

PICCS : Prior-Image Constrained Compressed Sensing

PTV : Planning Target Volume

SI : Superior-Inferior

SM : Setup Margin

TCGM : Time-ordered Chain Graph Model

TVCS : Total Variation-based Compressed Sensing

VMAT : volumetric modulated arc therapy

XVI : the X-ray Volume Imaging

3D : three-dimensional

4D : four-dimensional

Contents

1. Introduction

1.1. Radiotherapy and the definition of its target volume

Radiotherapy is one of three main cancer treatment approaches as well as surgery and chemotherapy, and approximately 50 % of all cancer patients seem to be treated by external beam radiotherapy in the world [1]. In order to implement adequate radiotherapy, treatment target volumes should be delineated on the planning CT image volumes. The definition of target volumes was defined and issued by the International Commission on Radiation Units and Measurements (ICRU) as ICRU report 50 and 62 [2], [3], which are shown in Fig. 1.1: Gross Tumor Volume (GTV), Clinical Target Volume (CTV), Internal Target Volume (ITV), and Planning Target Volume (PTV). ITV is defined as the region where CTV could move, and the margin between CTV and ITV is called Internal Margin (IM). PTV is also defined as the region that ITV could be fluctuated because of patient-setup uncertainty in each treatment day, and the margin is called Setup Margin (SM). SM is derived by geometrical deviation of patient setup, which consists of random component and systematic component [4], [5].

The dose concentration to the targeted area is nowadays highly achievable with sparing the normal tissues by employing the intensity-modulated radiotherapy

(IMRT). However, because the prescribed dose is escalated, the IMRT requires very high confidence in target localization by managing daily setup variability and intra-fraction motion during beam delivery. In addition, if patient-setup uncertainty is able to be kept small for all patients' case, SM and therefore PTV can be made smaller, thus the region where high dose will be delivered can be made smaller. This is obviously beneficial for patients and is the origin of the needs for image-guided radiotherapy (IGRT) which will be discussed later in this chapter.

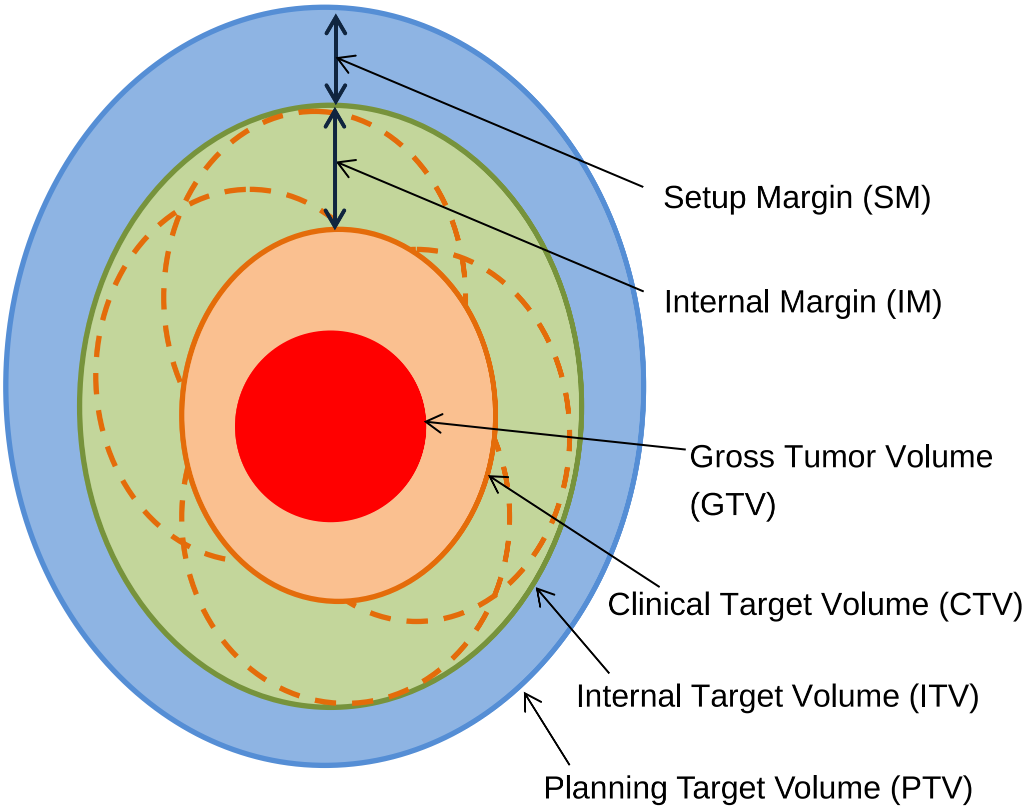

Figure 1.1: Definition of treatment target volumes [2], [3]

1.2. Intensity-modulated radiotherapy and image-guided radiotherapy

Radiotherapy treatment has always been asked the question: how to deliver prescribed dose only to the treatment target with less radiation damage to the adjacent normal tissues. As mentioned in the previous subsection, two radiotherapy techniques have provided the answer for the question: intensity-modulated radiotherapy (IMRT) and image-guided radiotherapy (IGRT). IMRT technique with multi-leaf collimator (MLC) unit and treatment planning software using inverse planning algorithm enables to deliver prescribed dose to the treatment target appropriately, and at the same time to preserve adjacent normal tissues from unexpected irradiation [6]–[9]. IMRT has been reported to improve disease control without critical side effects for nonmetastatic prostate cancer patients, compared to conformal radiotherapy [10]. The technique makes concentrated high dose area in the target volume and steep dose gradient around the target, as shown in Fig. 1.2, but at the same time the technique inherently contains the risk to deliver concentrated high dose to the normal tissues if the position of the patient on the treatment couch is not correct. The improvement of the accuracy of patient setup was provided by IGRT technique with imaging devices, such as electric portal imaging device (EPID) and cone-beam computed tomography (CBCT) system, both mounted on linear accelerator gantry [11]–[15].

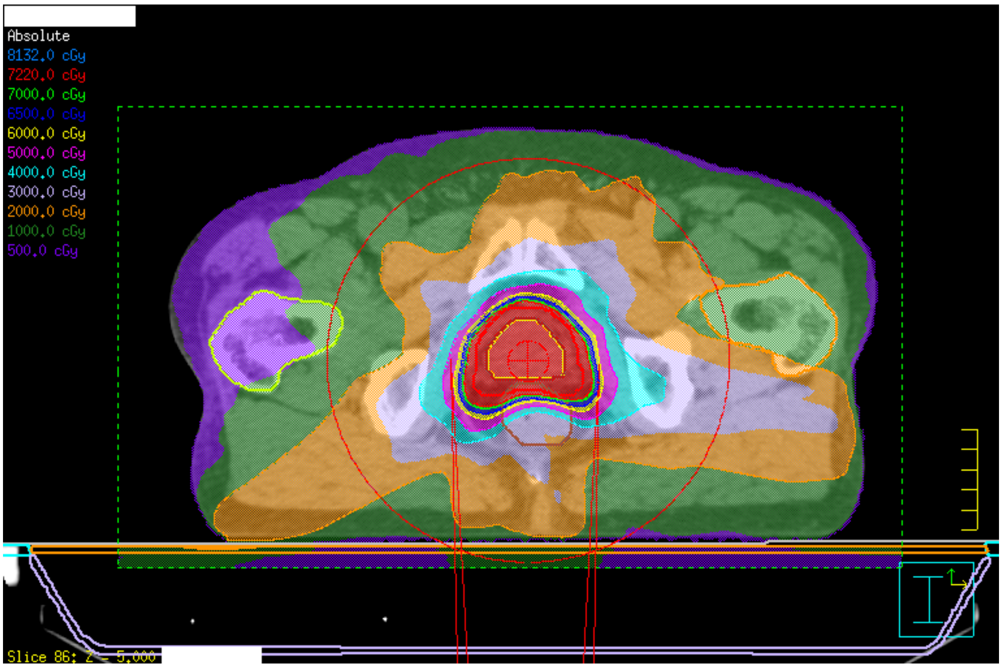

Figure 1.2: An example of IMRT dose distribution calculated by treatment planning software on treatment planning CT image set.

1.3. Cone-beam CT on medical linear accelerator gantry and improvement of patient-setup accuracy

Since introduced by Jaffrey *et al.*, CBCT technique has been taking very important role in IGRT approach [11], [16]–[18]. Fig. 1.3 shows cone-beam measurement system called the x-ray volume imaging (XVI) system, which consists of kilovoltage x-ray tube and flat-panel detector (FPD) unit perpendicularly to the treatment megavoltage beam, mounted on Synergy linear accelerator (Elekta, UK) gantry.

Having established this technique, the accuracy of patient setup, *i.e.* the accuracy of dose delivery, was dramatically improved. Before introduction of CBCT imaging system, an orthogonal pair of portal images of posterior-anterior (PA) and lateral direction using portal films or EPID device was taking main role in patient-setup workflow[14], [19], [20]. Little *et al.* (2003) reported that, using portal films and daily B-mode acquisition and targeting (BAT) ultrasound system, PTV margins for lateral, PA and superior-inferior (SI) were 5.3, 10.4 and 10.4 mm respectively [21], [22]. But after the introduction of CBCT system, Shiraishi *et al.* (2014) reported that PTV margins can be reduced to 5 mm [23]. This margin included the causes due to the insufficient correction of the day-by-day target displacement and the internal motion of the target.

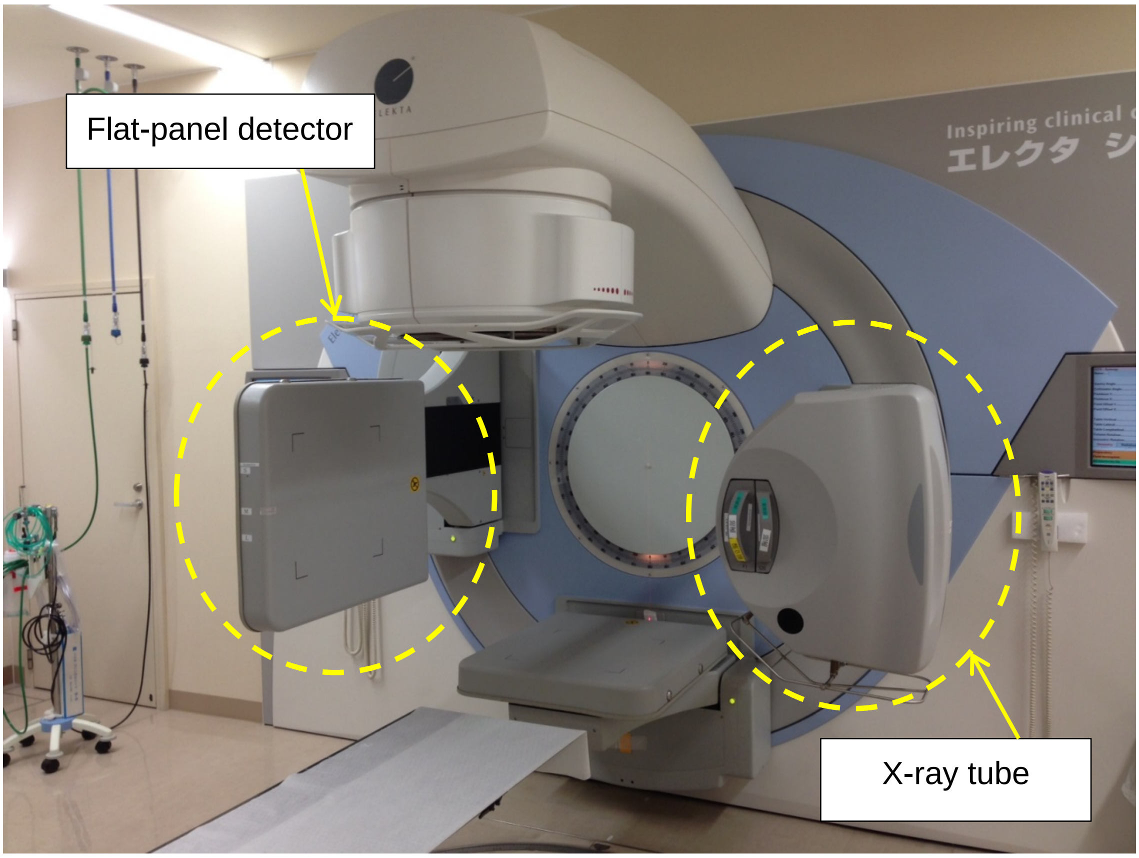

Figure 1.3: Synergy linear accelerator and XVI system mounted on Synergy gantry. A pair of X-ray tube and flat-panel detector locates perpendicular to the direction of treatment MV beam.

1.4. Two types of motion of the treatment target: interfractional and intrafractional motion

The positional accuracy of the treatment target is affected by the displacement of tumor inside the body of a patient. There are two types of tumor displacement: interfractional displacement and intrafractional displacement [24]. The displacement between treatment sessions, *i.e.* day-by-day displacement after patient registration, is regarded as interfractional motion, whereas the displacement during one treatment session is regarded as intrafractional displacement. It is easily imagined that the location of lung tumor might move in the body of the patient because of respiratory motion, and it is classified as periodic intrafractional motion. Gastrointestinal peristaltic action and rectal wall deformation caused by the action could be also classified into intrafractional motion[25]–[27], but it is non-periodic one. Shirato *et al.* (2004) pointed that the improvement of IGRT provides large reduction of interfractional uncertainty of tumor position control and the next step is to deal with intrafractional location accuracy [28].

In recent years, IGRT technique with CBCT system has also developed for periodic intrafractional motion of treatment targets, such as lung tumor and liver tumor. Sonke *et al.* (2009) and Nakagawa *et al.* (2013) demonstrated and proposed stereotactic volumetric modulated arc therapy (VMAT) for lung tumor combined with 4D CBCT image series to improve patient setup accuracy even if the treatment target was accompanied with respiratory tumor motion [29], [30]. The proposed method reconstructed 4- or 10-phase 4D CBCT image sets of lung tumor and the position of lung tumor was confirmed visually by comparing imported PTV contours and 4D movie of reconstructed CBCT images on the same display. For non-periodic intrafractional organ motion, on the other hand, no attention has been paid in IGRT using CBCT system, in spite of the fact that it was observed by the other systems, such as a Calypso device [31][32].

1.5. Four dimensional organ motion and its CBCT imaging

1.5.1. Periodic organ motion and its impact for dose delivery

Periodic organ motion includes respiratory motion of lung, liver and esophagus, and cardiac activity, and the motion of lung tumor has been focused for many years. Shirato *et al.* (2004) described lung tumor motion using power function of cosine [28]. Yamashita *et al.* (2011) studied the respiratory motion of esophageal tumor using 320-row multidetector CT, and reported the maximum esophageal tumor travel caused by respiration was 16.3 mm in cranial-caudal direction [33]. Mechalakos *et al.* (2004) discussed dosimetric impact caused by respiratory motion and reported that dose to 95% of the GTV and volume of the GTV receiving 95% were both reduced -9.8 % and 8.3 % respectively by the effect of normal breath comparing to the case without breathing [34].

For the purpose of 4D CBCT image reconstruction accompanied by periodic organ motion, such as respiration and cardiac activity, information about respiratory phase or cardiac motion signal is necessary to classify projections into several phase groups. In the case of respiratory motion, the measurement method of a signal synchronized with projection images is categorized by two methods; the use of an external respiratory or cardiac monitoring system and the image-based respiratory phase recognition. For example of the latter case, Sonke *et al.* (2005) proposed the method known as Amsterdam Shroud, which produces 1D projection in cranio-caudal (CC) direction after applying CC derivative filter [35], and this has been used in the commercial CBCT device (Elekta Synergy). Regarding cardiac activity, Lauzier *et al.* (2012) demonstrated 4D image reconstruction using the electrocardiogram (ECG) signals in order to sort projections into several cardiac phases [36], which is categorized into the former case.

1.5.2. Non-periodic organ motion and its impact for dose delivery

Many organs located in lower abdominal and pelvic region are also known as moving organs. Not only interfractional displacement, several studies discussed about intrafractional displacement of prostate grand. Langen *et al.* (2008) reported the measurement results of intrafractional prostate motion for 17 patients using the Calypso four-dimensional localization system [31]. They reported that the averaged value of the largest displacement for 17 patients was 6.1 mm in posterior-anterior direction. Kupelian *et al.* (2007) reported clinical experience of treatment target localization using Calypso system and mentioned its clinical efficiency [32].

Moreover, the difficulty caused by the presence of rectum and other digestive tract are making the problem of prostate displacement more complex. Zelefsky *et al.* (2002) studied rectal toxicity of prostate IMRT radiotherapy, and reported that toxicity rate reduced by application of IMRT in comparison with conformal radiotherapy, but still 4.5 % of treated patients experienced acute rectal toxicity [37].

There are some proposed preparative regimens to deal with positional changes of prostate. It is better to be kept the size of bladder and rectum consistent throughout treatment course, and patients are instructed to ingest repeatable amount of water and to empty their bowels prior treatment sessions [22], [38]. Teh *et al.* (2001) reported their clinical experience using rectal balloon and mentioned two advantages, prostate immobilization and reduction of rectal toxicity [39]. Those preparative regimens are regularly treated, but intrafractional motion cannot be perfectly eliminated and toxicity has still reported as mentioned above.

Though many researchers have mentioned about intrafractional displacement around pelvic region, only few studies have dealt with CBCT volumetric imaging with non-periodic intrafractional motion or deformation in radiotherapy. One of the approaches for 4D reconstruction of time-ordered non-periodic motion is known as short-scan / half-scan reconstruction. Regarding to the concept of short-scan CT image reconstruction, its temporal resolution and continuous time-ordered image reconstruction has been focused and discussed by Parker *et al.* (1982), Noo *et al.* (2002), and Liu *et al.* (2001) [40]–[42]. In this approach, temporal resolution is directly related to the rotation speed of the measurement geometry and the angular range, and the shorter range surely provides its better temporal resolution. However, the shorter range of projection might cause degradation of image quality and artifacts if the range is shorter than 180 degrees plus fan-angle [42], [43]. On the other hand, Pang and Rowlands (2005) and Godfrey *et al.* (2006) introduced ‘just-in-time tomography’ which reconstructs digital tomosynthesis images from projections of cone-beam acquisition geometry [44], [45]. The method was really time-ordered imaging approach but the created tomosynthesis images were still two-dimensional.

1.6. Adaptive Radiotherapy

The impact of inter- and intrafractional organ motion and deformation is discussed in the subsections above, and one more new and important concept should be introduced in this subsection, namely, adaptive radiotherapy, which is a radiotherapy workflow containing feedback process of dosimetric consequence until previous treatment session, as shown in Fig. 1.4 [46]–[49]. The concept of adaptive radiotherapy was firstly introduced for the purpose of reducing treatment target margins from the feedback of actual setup accuracy in order to spare adjacent normal organs [46], [48], but it was extended into more active treatment process with accumulation of already delivered dose distribution and modification of treatment plan with daily- or weekly-updated image sets of a patient [47], [50]–[53]. In this context, daily CBCT image acquisition and 4D CBCT reconstruction have been taking a new role in adaptive radiotherapy workflow for the purpose of understanding more accurate dose distribution considering inter- and intrafractional motion and deformation. To feedback dose distribution considering interfractional motion, daily imaging step in Fig 1.4 provides anatomical information of the treatment day, as Ding *et al.* (2007) and Yang *et al.* (2007) proposed [54], [55]. To deal with intrafractional motion and deformation, in-treatment CBCT acquisition contributes to provide intrafractional volumetric image, as proposed by Kida *et al.* (2012) [56]. Thus, nowadays imaging techniques in radiotherapy field have been required, not only for the purpose of patient setup or initial treatment planning, but also for the purpose of adaptive radiotherapy implementation.

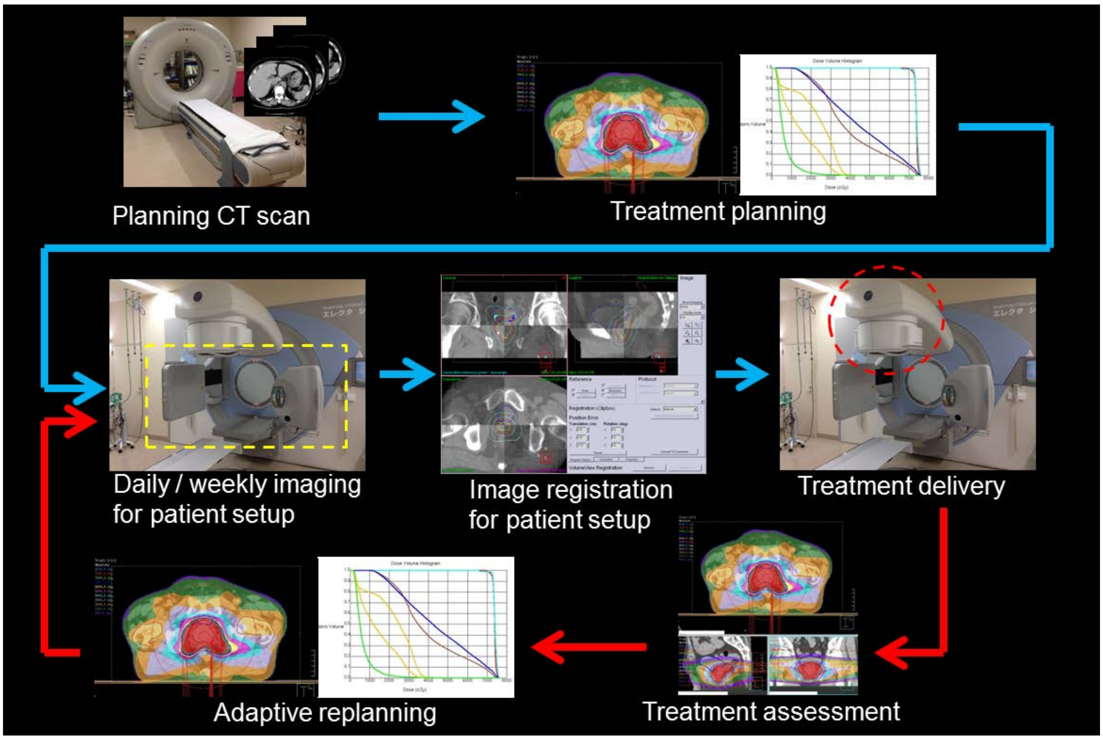

Figure 1.4: Workflow of adaptive radiotherapy. Radiotherapy workflow is commonly starting from acquisition of planning CT image sets and treatment planning, then the treatment delivered after registration step using daily/weekly imaging. The workflow of adaptive radiotherapy contains feedback process of treatment delivery and replanning of future treatment fractions.

1.7. Reconstruction techniques

It is no doubt that the development of CT reconstruction algorithm was a great innovation. The innovation made a huge impact for not only Radiology field but also other clinical departments, and it deserved the Nobel Prize in Physiology and Medicine 1979 [57], [58]. From 1980's to early 2000's, filtered back projection (FBP) reconstruction technique was the main reconstruction scheme because of the benefit of calculation acceleration using fast Fourier transform (FFT) even if computational environment was not powerful enough [59]–[61]. Regarding cone-beam projection geometry, it was developed straightforwardly by Feldkamp, Davis and Kress, so called FDK algorithm, which is still popular in clinical use [62]. In this thesis, this algorithm combined with the convolution formalism derived by Webb (1982) was applied for non-periodic cone-beam image reconstruction of the study discussed in Chapter 2 [62], [63].

With the development of computer resources, the other approach recently becomes available in practice; iterative reconstruction approach, which is categorized by algebraic reconstruction technique (ART) and statistical approach such as maximum *a posteriori* probability (MAP) methods [59], [64]. The concept of iterative reconstruction was introduced in the early stage of tomographic image reconstruction development [65], [66], however, although it was used in the field of nuclear medicine because of much less number of projections, physicians and physicists needed to wait for huge improvement of computational resources for a few decades, to be ready for iterative CT and CBCT image reconstruction.

1.8. Iterative reconstruction technique

In recent year, iterative reconstruction technique has been focused again, caused by the huge progress of computational resource, especially by use of graphics processing unit (GPU) [67]–[70]. Iterative reconstruction approach consists of ART and statistical approach such as MAP methods. The former method is simply repeating to solve algebraic equations and to update image pixel values [59], [65], [71]. The latter one is based on the theory that the measurement of photon obeys Poisson probability distribution, combined with the maximization process to maximize *a posteriori* probability using Bayesian theorem to use known prior information [71]–[74].

One of the great advantages using MAP reconstruction algorithm is that the image reconstruction works even with the limited number of projections[75], [76]. To obtain the non-periodic time-ordered images, the projection data should be classified by time-ordered phase bins. The projection angle range in each time phase has to be as narrow as possible, much less than 180 degrees plus fan-angle range requiring in FDK algorithm, to assure the high time resolution in the reconstructed images.

In this thesis, iterative reconstruction based on MAP method is employed to reconstruct image from narrower projection range and initial image sets, in order to improve temporal resolution, then the feasibility of new concept considering time-ordered image series is discussed.

1.9. Purpose of this thesis

As mentioned in the previous subsections, the study of four-dimensional volumetric visualization focusing on non-periodic time-ordered organ motion / deformation is quite limited. However, it is important to understand the impact of non-periodic organ motion for accurate dose delivery of radiotherapy as well as the case of periodic motion. The aim of this research is to deal with 4D reconstruction of CBCT imaging accompanying non-periodic time-ordered organ motion.

In the first part of this thesis, short-scan FDK approach is applied for the 4D reconstruction, and then the limitation of temporal resolution regarding FDK approach for time-ordered 4D reconstruction are discussed. In the second part of the thesis, MAP iterative reconstruction approach is applied for time-ordered 4D reconstruction, and the new concept, time-ordered chain graph model, is introduced and employed to use narrower angular projection range for the reconstruction, which aims to improve temporal resolution.

2. Time-ordered 4D CBCT reconstruction using Short-Scan FDK method

2.1. Introduction to Chapter 2

The feasibility of time-ordered 4D CBCT reconstruction using short-scan approach with FDK method is discussed in this chapter, using projections of clinical patients and virtually created digital phantom. As mentioned in the introduction chapter, FDK method is categorized in analytical approach, and recognized as an extended method of filtered back-projection (FBP) method [59], [62]. The advantage of FDK approach is sharpness of the reconstructed images and its reconstruction speed, but it also has a drawback which is the requirement of projection angle range, *i.e.* projection range of 180 degrees plus fan-angle is needed for image reconstruction [40], [41], [77]. This issue causes tradeoff between temporal resolution and image degradation in 4D reconstruction. This tradeoff is discussed in this chapter, especially using virtually created digital phantom projections.

Additionally, there is one more problem to be solved for time-ordered 4D short-scan FDK reconstruction for clinical patient data: truncation of projections contained in cone-beam projection measurement. In the case of abdominal and pelvic CBCT acquisition, a flat-panel detector (FPD) is usually located asymmetrically in order to cover whole abdomen or pelvis in one rotation of the gantry [78]. In other words, acquired projections even with 180 degrees plus fan-angle range are incomplete for whole-body reconstruction. Therefore, the visible area of reconstructed image should be limited and strong artifacts must be caused by truncation if short-scan FDK reconstruction is implemented without taking care of it. This problem is also discussed in this chapter and projection extension method using image mosaicing technique is introduced, followed by the discussion of the feasibility of time-ordered short-scan FDK CBCT reconstruction.

2.2. Materials and methods

2.2.1. Projection data used in this study and projection geometry

Two kinds of projection data sets were used for cone-beam CT image reconstruction in this study; the digital phantom projections which contain a moving air sphere, and clinical patients' data sets. Figs 2.1 (a) to (d) show cone-beam kilovoltage projection geometries of the XVI system (Elekta, UK). The XVI system consists of x-ray projection source and FPD with 512×512 detector elements, which is mounted on the gantry of Synergy linear accelerator (Elekta, UK) [16], [18]. The projection direction of the XVI system is perpendicular to the direction of treatment megavoltage beam. There are three options of FPD location depends on the size of the patient or the scanned object [78], and usually S mode is used for head-and-neck region and M mode for abdominal and pelvic regions as shown in Figs. 2.1 (b) and (c). The digital phantom projections are virtually created according to the geometry of S mode with centered FPD panel, shown as Fig. 2.1 (b), and patient data sets used in this chapter were acquired in the M mode geometry with 11.5 cm offset located FPD panel as shown in Fig. 2.1 (c).

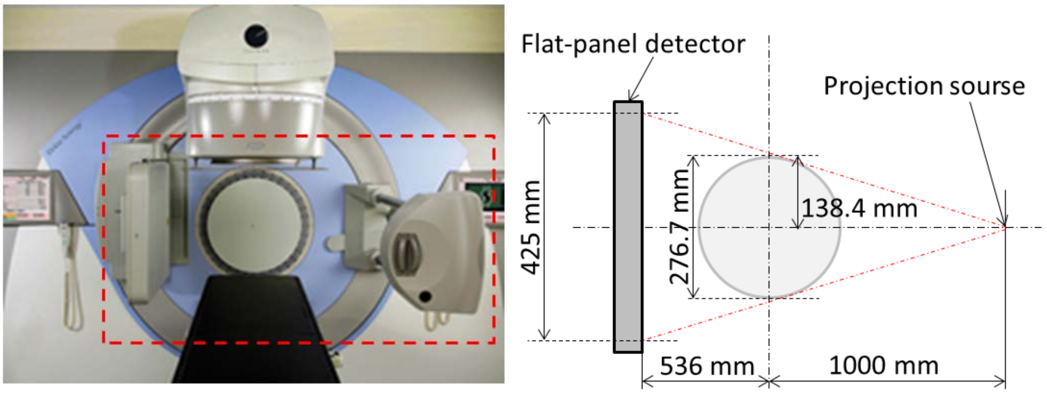

(a) The XVI system

(b) S option for small FOV (27 cm)

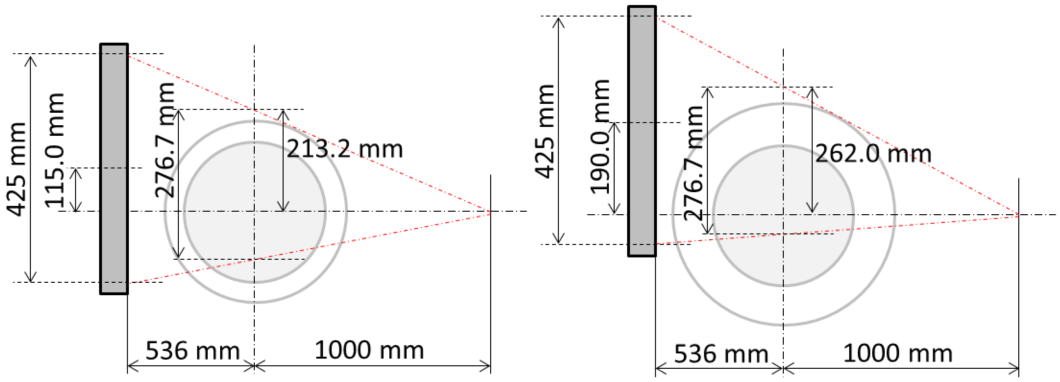

(c) M option for medium FOV (41 cm)

(d) L option for large FOV (50 cm)

Figure 2.1: Cone-beam projection geometry of the XVI system [78]. (a) Overview image of the XVI system, (b) geometry of S option for 27 cm FOV, (c) geometry of M option for 41 cm FOV and (d) geometry of L option for 50 cm FOV.

2.2.2. Digital phantom and its projection data

Figs 2.2 show the schematic diagrams of elliptic-cylindrical digital phantom and its projection geometry. The cone-beam projection data containing an air sphere were virtually created in one-degree interval for 360° which corresponds to one rotation of the measurement geometry around the phantom. The geometry was same as that in S mode of the XVI system shown in Fig. 2.1 (b). The diameter of the air sphere was set to 3 cm and the sphere moved 3 cm in longitudinal direction, which corresponds to z direction in Fig. 2.2 (a), during one rotation of the projection source with constant speed and without deformation. The diameter and travel distance of an air sphere in the digital phantom were defined based on the observed result of one patient's projection set.

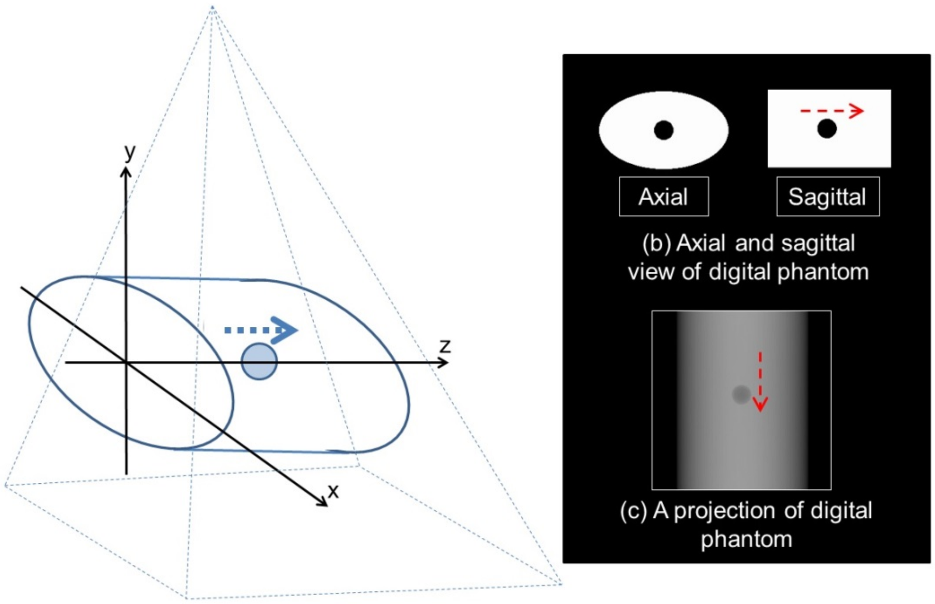

(b) Axial and sagittal view of digital phantom

(c) A projection of digital phantom

(a) Schematic diagram of digital phantom and projection geometry

Figure 2.2: Schematic diagram of digital phantom containing moving air sphere. Figure (a) shows the geometry to create digital phantom projection, (b) shows axial and sagittal image of original digital phantom and (c) is one of virtually created projections. An air sphere of 3 cm diameter moves 3 cm in z-axis in (a) during one rotation of projection source.

2.2.3. Patients' projection data sets

Clinical patients' projection data sets were acquired using the XVI system. Those were acquired as pre-treatment CBCT imaging for the purpose of patient-setup for prostate radiotherapy. Two clinical projection data sets were used in this study and their acquisition durations were about 120 seconds for patient A, and 60 seconds for patient B. The data sets were collected with M FOV option which requires 11.5 cm offset location of FPD unit as shown in Fig. 2.1 (c), and the projections contained truncation as shown in Fig. 2.3.

Normally pelvic CBCT reconstruction requires completely one rotation of measurement geometry in order to cover whole of pelvic region. However, this study is dealing with short-scan and the truncation in projections could cause problems. To overcome this problem, projection extension process is introduced in the later subsection.

Figure 2.3: An example of projection of pelvic region with FPD position M, acquired by the XVI system.

2.2.4. Time-ordered short-scan FDK reconstruction

CBCT volumetric image sets were reconstructed using in-house software based on FDK method. As shown in Fig. 2.1 (a), the direction of cone-beam projection acquisition using the XVI system is perpendicular to the treatment megavoltage beam. The measurement starts from 9 o'clock position and the measurement geometry rotates counter-clockwise direction. Fig. 2.4 shows the schematic sequence of cone-beam projection acquisition and the projection ranges for sequential short-scan FDK reconstruction. Assuming image reconstruction of FOV 40 cm using M option of FPD location, projection range of 200°, which is equal to 180° plus fan-angle in this geometry, is required for each time phases, so the first image can be reconstructed using projections from the started position of the measurement until rotation angle of 200°. Then the projection range slides towards the direction of rotation with keeping the width of the range until the end of the range reached to the end position of the rotation.

In the first part of this study, the digital phantom image sets were reconstructed with several projection ranges less than 200 degrees, then the degradation of images and temporal resolution are discussed using the shape of moving air sphere. In the second part, reconstruction of clinical patients’ 4D image sets was implemented using projections with angular range of 200° and the feasibility of this method is discussed.

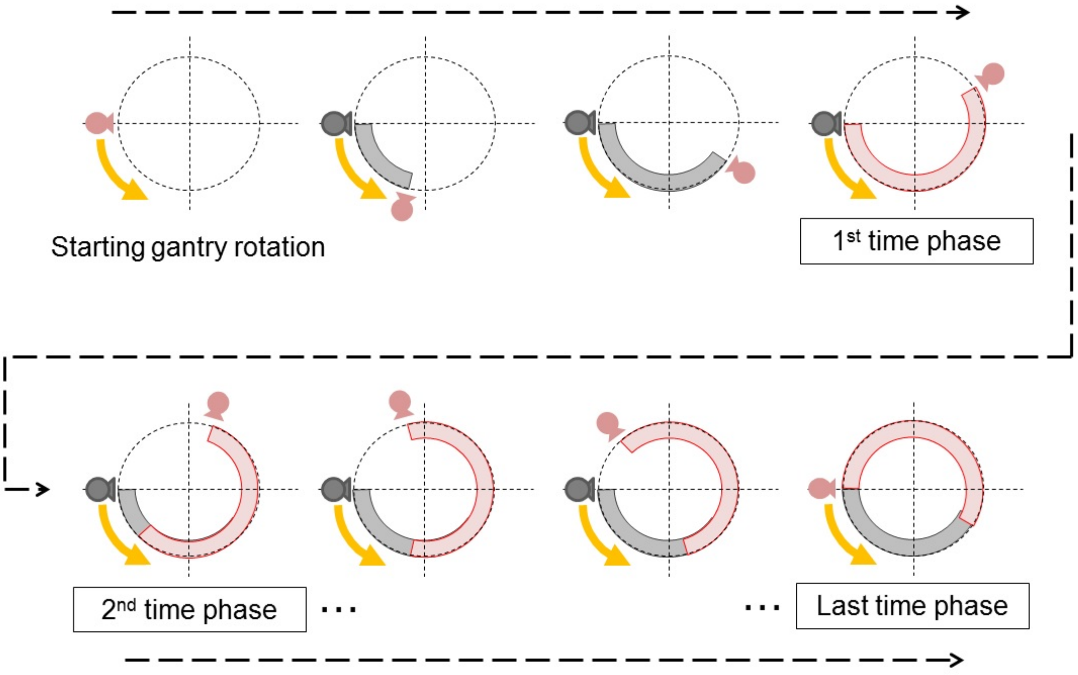

Figure 2.4: Schematic workflow of gantry rotation and projection range of time-ordered FDK reconstruction. Gantry rotates CCW direction and projection range for image reconstruction slides as the time phase progresses.

2.2.5. Projection extension using mosaicing process

Time-ordered 4D short-scan FDK reconstruction method is introduced in the previous subsection. The method was directly able to apply for the digital phantom projections because they were assuming S FOV option which did not contain truncation. On the other hand, clinical projections which were acquired in M FOV option contain truncation and it must cause strong artifact. Fig. 2.5 (a) shows reconstructed FOV using truncated projections measured by M FOV option, and the range of projections is 180°, and the reconstructed image is shown as Fig. 2.5 (b). In order to reconstruct full FOV with short-scan reconstruction workflow, extended projections and angular range of 180° plus fan-angle are required as shown in Figs. 2.5 (c) and (d).

In this subsection, the method to extend truncated projection using image mosaicing process in order to reconstruct time-ordered 4D images without truncation artifact is proposed. Image mosaicing process itself is widely used in the field of computer graphics to create wider images using several smaller images [79]–[82]. In the present study, extended projections are created by combining this mosaicing technique with reprojections from the images reconstructed with whole projection data.

The proposed method to extend truncated projections is schematically shown in Fig. 2.6, which consists of the following three steps: step i) reconstructs normal 3D CBCT images using 360-degree projections with 512×512 detector elements (Fig. 2.6 (a) and (b)), then step ii) makes virtual reprojections with 512×800 detector elements, which are wider than original projections and contain whole of abdominal or pelvic region in transverse direction (Fig. 2.6 (c)), and step iii) combines original projections with virtual reprojections into extended ‘mosaic’ projections (Fig. 2.6 (d)). Note that the pixel values of the original projections were adopted if pixel values on both original projections and reprojections existed at the same pixel of the projection.

For the purpose to prevent unexpected irradiation for outside of interested region, the collimator made by lead was inserted just under the x-ray source and it created blocked region on the projections. But the blocked region creates artifacts on the reprojections just inside of the blocked region. Therefore, padding process was implemented in the step i) for blocked region in the projections before normal 3D reconstruction, as shown in Fig. 2.7.

The truncated “missing” regions in original projections were extended using virtually created reprojections in the step iii), shown as Fig. 2.6 (d). Fig. 2.8 shows more details about the step iii), where the padded original projection was combined with virtually created reprojection to create “mosaic” projections. As mentioned above, the pixel values of the original projections were adopted if original projections existed at the interested area.

Ideally, this mosaic process should work without any correction. Actually, however, this process needs correction of pixel value intensity for virtually created reprojections to prevent remaining non-contiguous boundary between original projection and “extended” virtual reprojection area. The pixel value correction is applied for virtual reprojections, shown as Fig 2.8 (b), where the correction is determined by a minimization process of $f(a, b)$ defined as below,

$$f(a,b) = \sum \left(x_{Real} - x_{AdjustedVirtual}\right)^2$$

$$= \sum (x_{Real} - (a x_{Virtual} + b))^2 \qquad (2\text{-}1)$$

$$\binom{a}{b} = argmin\,\{f(a,b)\} \qquad (2\text{-}2)$$

where x_{Real} and $x_{Virtual}$ are pixel values inside four yellow ROIs, 2×8-pixel regions as shown in Figs. 2.7 (a) and (b), for both real projection and virtual reprojection, respectively. $x_{AdjustedVirtual}$ represents pixel values after correction and it was assumed to be described as a linear function using parameters a and b. This correction was performed for all projections acquired in the clinical case. The detailed derivation to determine a and b in Eq. 2-1 and 2-2 is given in Appendix A.

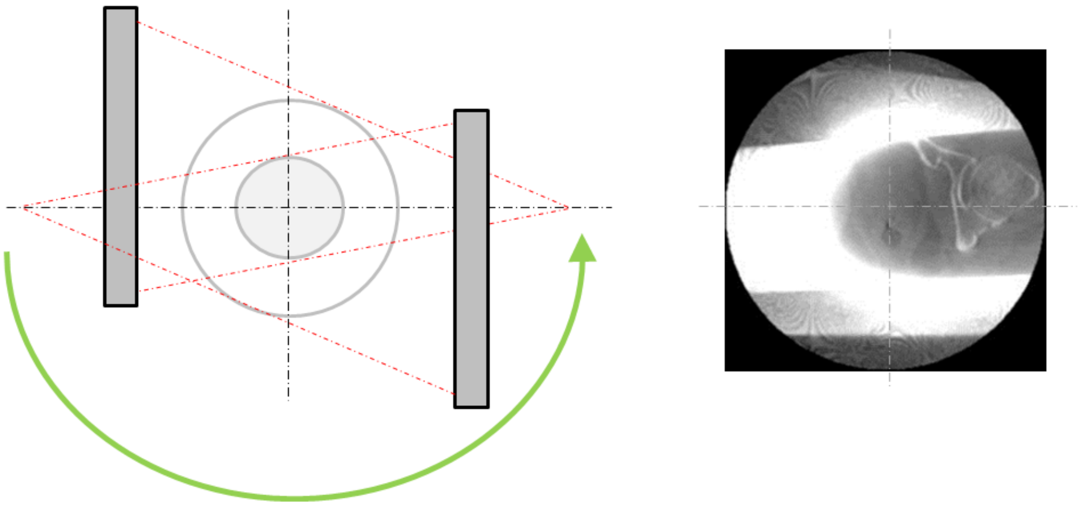

(a) Reconstructed FOV with M FOV mode and 180° angular range. The visible area is limited less than 127 mm-diameter.

(b) Reconstructed image using geometry (a)

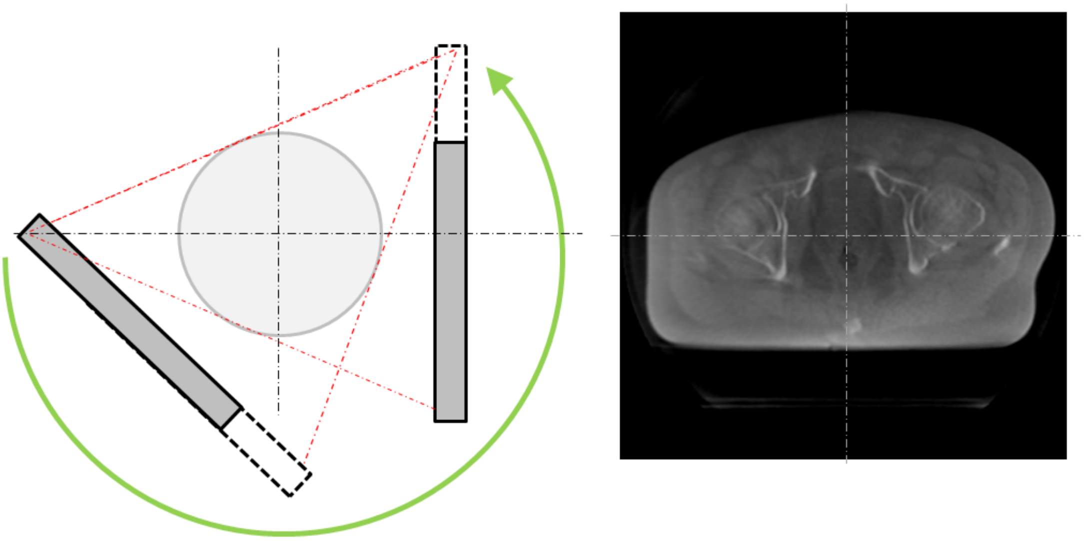

(c) Reconstructed FOV using extended projection and 200° angular range. Whole of 400 mm FOV is visible.

(d) Reconstructed image using geometry (c)

Figure 2.5: Schematic diagram of relationship between reconstructed FOV, shifted FPD and projection range. Figure (a) and (b) demonstrate the geometry and reconstructed image using projections of 180° range without extension. The image with full FOV, shown in (d) is reconstructed by extended projections and 200° projection range, shown in (c).

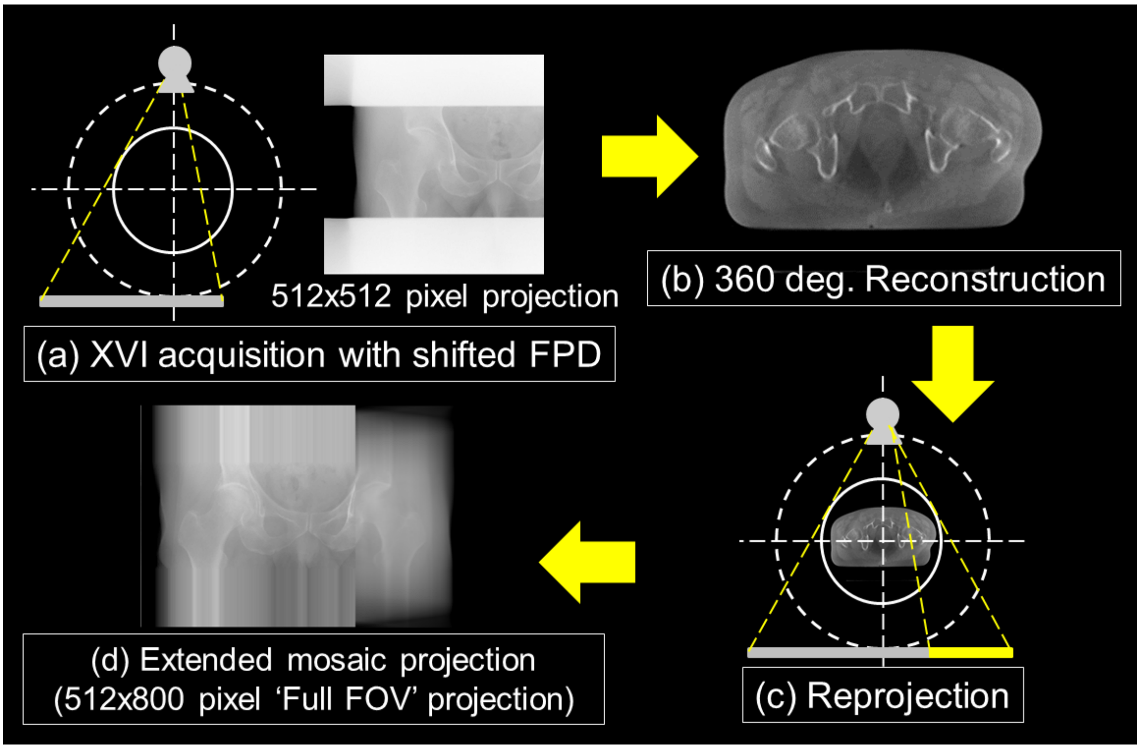

Figure 2.6: General workflow of truncated projection expansion. Firstly, 3D reconstruction (b) was implemented using non-extended original projections (a) of all 360° range, then reprojections (c) were created virtually from image (b). Finally original projections (a) and reprojections (c) were combined and extended mosaic projections (d) were created.

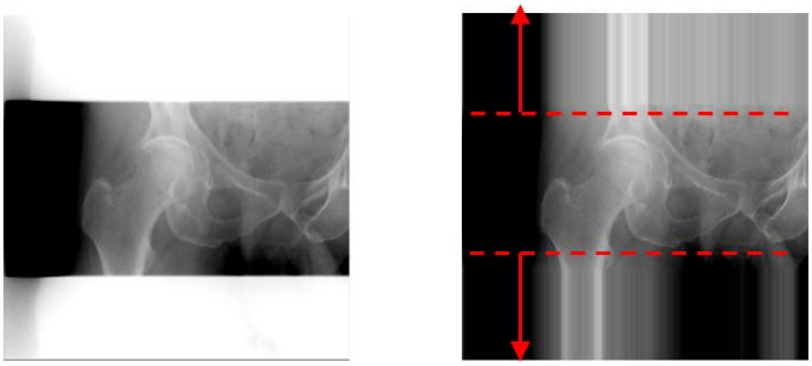

(a) Original projection (b) Padded projection

Figure 2.7: (a) Original projection and (b) padded projection.

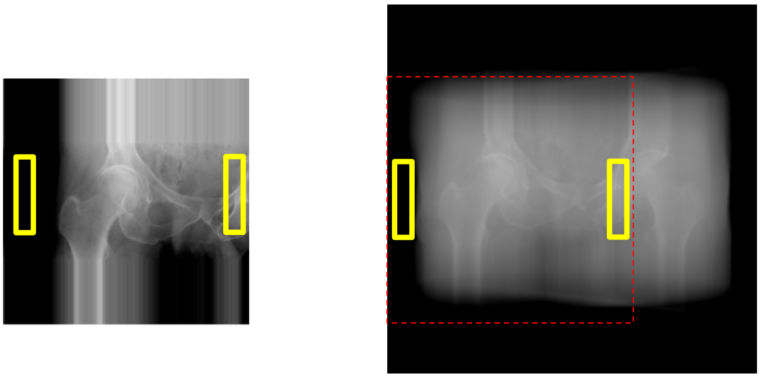

(a) Padded original projection (b) Virtual reprojection

Figure 2.8: (a) Padded original projection and (b) virtual reprojection. Yellow rectangular ROIs show the areas used for pixel value correction, and red dashed ROI shows the area which overlaps with padded projection (a).

2.2.6. Reconstruction implementation details and evaluation method of digital phantom

Image reconstruction was implemented using time-ordered short-scan FDK method for seven time-phases for both digital phantom cases and clinical patients' cases. The size of reconstructed digital phantom volume was 256×256 pixels in axial cross-section and 128 slices in longitudinal direction, with 1 mm voxel size. For all seven phases, three cases of angular projection range are chosen: 100°, 140° and 180°, and the center location of angular range is same for all cases of projection ranges. Further details are indicated in Table 2.1.

It is already known that the image reconstruction required projection ranges of at least 180° plus fan-angle, but on the other hand, temporal resolution might be improved as projection range is narrower. The relationship between temporal resolution and degradation of reconstructed images of digital phantom is evaluated by two methods: pixel value analysis on longitudinal axis profile and bounding box analysis. For the pixel value analysis, the profile was inversed and then normalized by maximum values. Bounding box analysis is the method to measure transversal, vertical and longitudinal size of the air sphere using virtual cube. The full widths of half maximum (FWHM) of pixel values in each axes are chosen as the length of the cube, for images of fourth time-phase out of seven.

In the case of patients' projection data sets of pelvic region, firstly image mosaicing process using original projections and virtual reprojections were implemented, then the extended projections were used for time-ordered short-scan FDK reconstruction with angular projection range of 200°, which is equal to 180° plus fan-angle in this reconstruction geometry. The reconstruction was implemented for five time-phases with 400×400 pixels in axial cross-section and 128 slices in longitudinal direction with voxel size of 1 mm, same as digital phantom case.

Table 2.1: The detailed angular range for time-ordered short-scan FDK reconstruction

Angular projection range	Number of time-phase	Start angle	End angle	Center angle of projection range
100°	1	40°	140°	90°
	2	70°	170°	120°
	3	100°	200°	150°
	4	130°	230°	180°
	5	160°	260°	210°
	6	190°	290°	240°
	7	220°	320°	270°
140°	1	20°	160°	90°
	2	50°	190°	120°
	3	80°	220°	150°
	4	110°	250°	180°
	5	140°	280°	210°
	6	170°	310°	240°
	7	200°	340°	270°
180°	1	0°	180°	90°
	2	30°	210°	120°
	3	60°	240°	150°
	4	90°	270°	180°
	5	120°	300°	210°
	6	150°	330°	240°
	7	180°	360°	270°
200°	1	0°	200°	100°
	2	40°	240°	140°
	3	80°	280°	180°
	4	120°	320°	220°
	5	160°	360°	260°

2.3. Results

2.3.1. Digital phantom results

Time-ordered 4D image sets of digital phantom were reconstructed using short-scan FDK method. Reconstructed images of fourth time phase out of seven, using 180-degree projection range and 100-degree projectin range, are shown in Fig. 2.9. In the case of 100-degree projection range, as shown in Fig. 2.9 (c), the elliptic outline of the phantom is not reconstructed properly, although the outline is reconstructed with 180-degree angular-range of projections as shown in Fig. 2.9 (b).

Normalized pixel-value profiles along longitudinal axis for three different projection ranges, 180-, 140- and 100-degree, are shown in Fig. 2.10, as well as reconstructed sagittal views. For all three cases, the full widths of half-maximum (FWHM) are all same but the profile of 100-degree projection range shows the narrowest penumbral width, which means the best temporal resolution among them.

Degradation of reconstructed image is also evaluated using bounding box analysis with FWHMs for reconstructed moving air sphere using 180-, 140- and 100-degree projection ranges, shown in Fig. 2.11. The FWHMs of air sphere in axial, sagittal and coronal planes are about 3 cm in the case of 180° for all time phases shown in Fig.

2.11 (b), whereas the widths show a large variation through all time phases in the case of 100° shown in Fig. 2.11 (d).

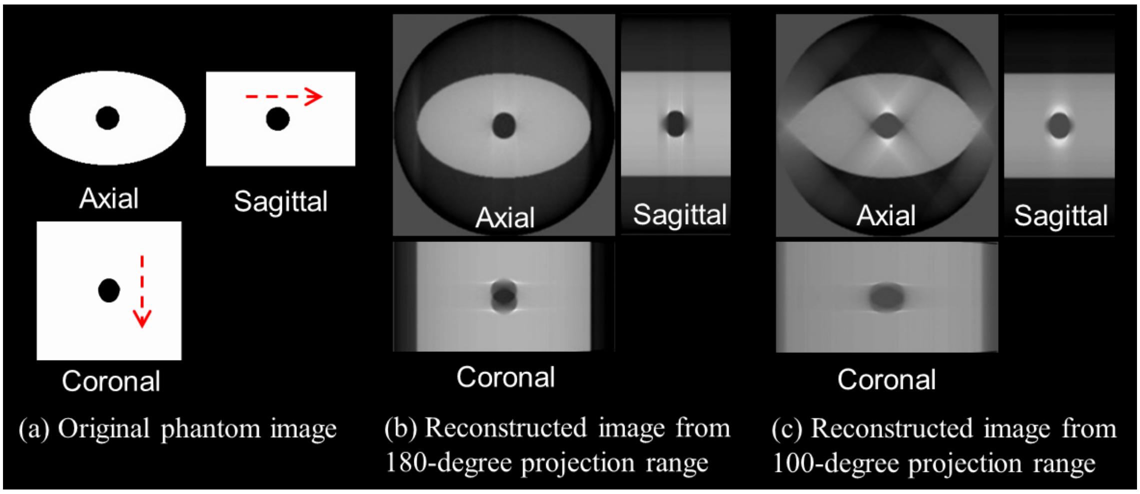

(a) Original phantom image (b) Reconstructed image from 180-degree projection range (c) Reconstructed image from 100-degree projection range

Figure 2.9: Axial, sagittal and coronal views of digital phantom images. (a) Images of original digital phantom. (b) Reconstructed images from 180° projection range. (c) Reconstructed images from 100° projection range.

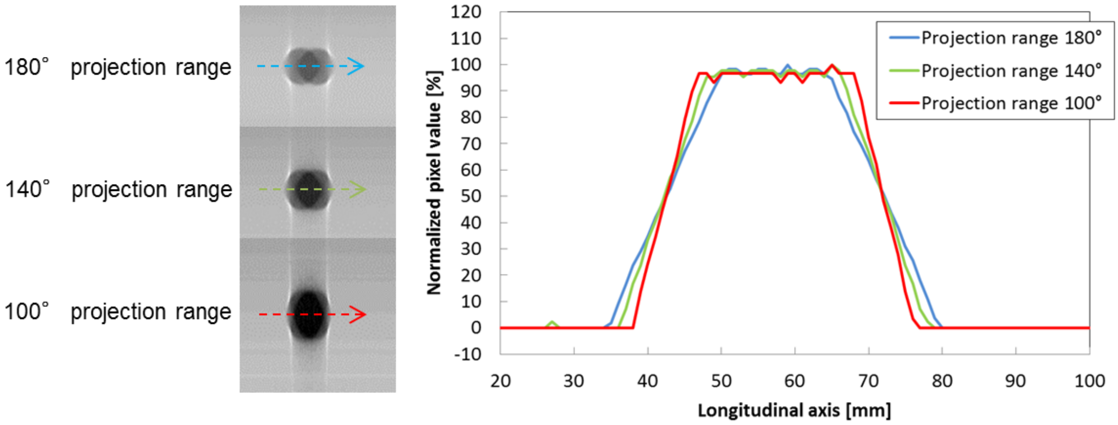

(a) Reconstructed sagittal images (b) Normalized pixel value profile

Figure 2.10: Sagittal images of moving air sphere reconstructed from 180°, 140° and 100° projection ranges, and their pixel value profiles along longitudinal direction.

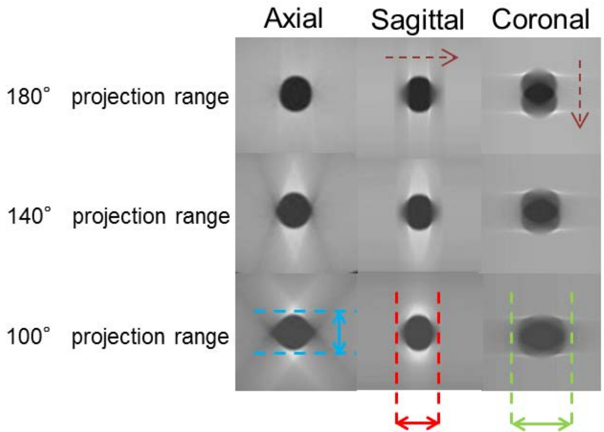

(a) Reconstructed images of moving air sphere

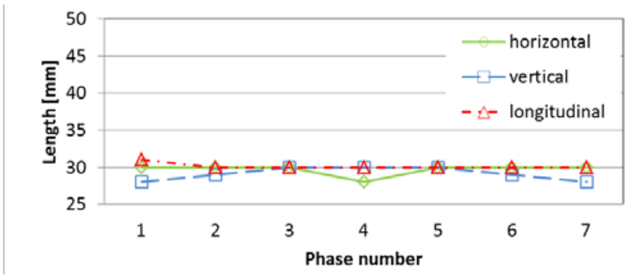

(b) Widths of air sphere, 180° projection range

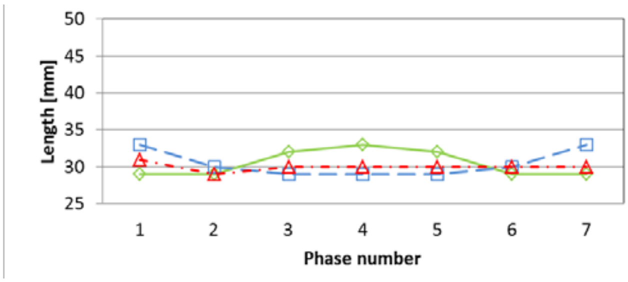

(c) Widths of air sphere, 140° projection range

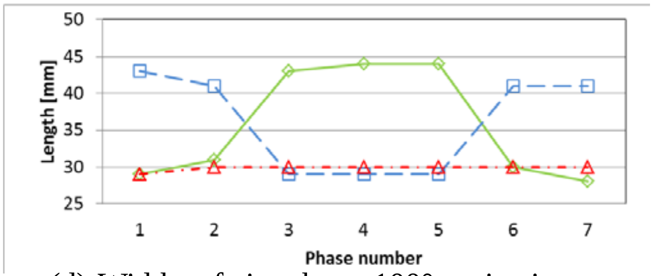

(d) Widths of air sphere, 100° projection range

Figure 2.11: Results of bounding box analysis for three reconstructed digital phantom image sets. (a) Axial, sagittal and coronal views of reconstructed images. Values of horizontal, vertical and longitudinal widths of (b) 180°, (c) 140° and (d) 100° range for each time phases.

2.3.2. Creation of extended mosaic projections

Figure 2.12 shows various projections in the middle of the process to create extended mosaic projection. Original projection shown in Fig. 2.12 (a) is padded and the projection without Pb blocked region is created as shown in Fig. 2.12 (b). In the mosaic process, padded projection (b) is combined with virtual reprojection (c), then extended mosaic projection is successfully prepared like Fig. 2.12 (d) for all projection angles.

In order to prevent remaining non-contiguous boundary between original projections and extended reprojections, minimization process of squared difference defined as $f(a,b)$ in Eq. (2-1) was implemented. Table 2.2 shows averaged values of squared difference per pixel, before and after correction. In both patient cases, squared difference values are diminished around 3000 per pixel.

Reconstructed images using 180-degree short-scan FDK method are also shown in Fig. 2.13, where the image reconstructed from original projections contains strong artifact caused by the truncation, whereas the artifact disappears in the one from extended mosaic projection.

Table 2.2: The squared difference values before and after correction

Patient	Squared difference value	
	Before correction	After correction
Patient A	70078.7	3085.3
Patient B	268421.3	2759.8

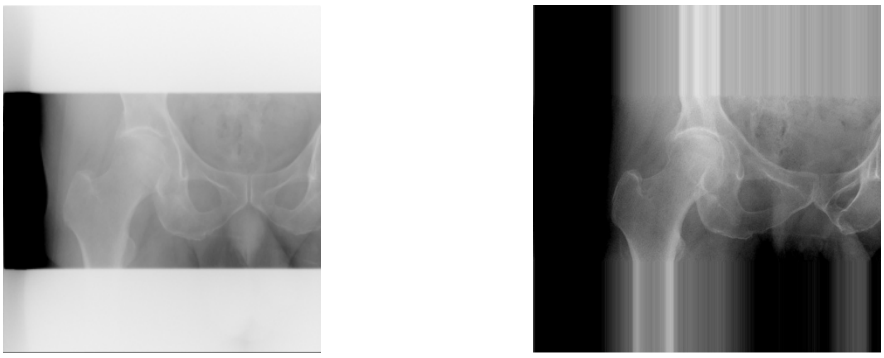
(a) Original projection

(b) Projection after padding

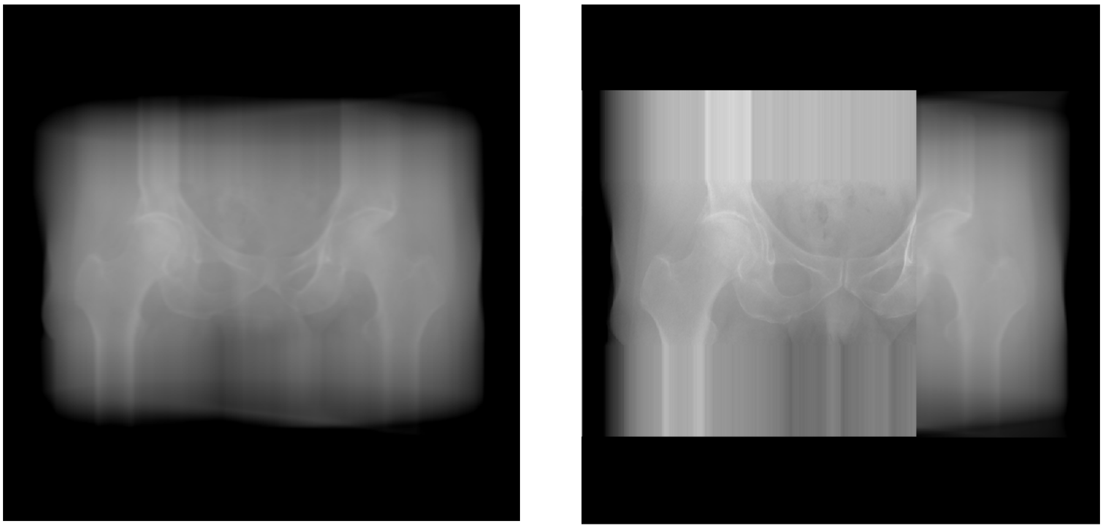
(c) Virtual reprojection

(d) Extended projection after mosaicing process

Figure 2.12: Projection image creation of pelvic region through mosaicing process to extend truncated projections. (a) Original projection, (b) padded original projection, (c) virtual reprojections and (d) extended mosaic projection.

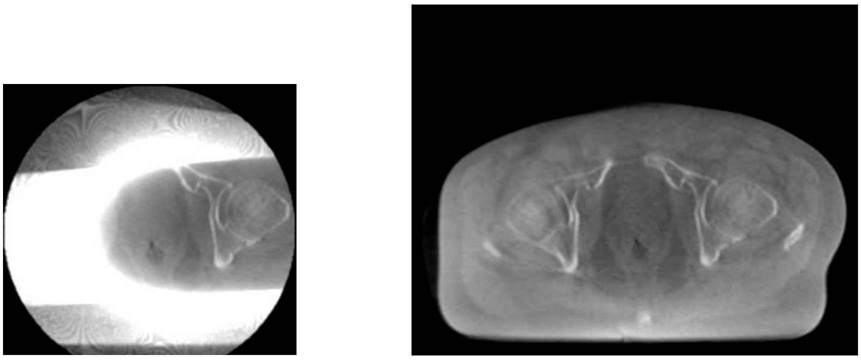

(a) Reconstructed from original projections

(b) Reconstructed from extended mosaic projections

Figure 2.13: Reconstructed images using 180-degree short-scan FDK method. (a) An image reconstructed from original projections and (b) an image reconstructed from mosaic projections.

2.3.3. Clinical patients' results of Time-ordered FDK reconstruction

Reconstructed images using clinical patients' projections of pelvic region using angular range of 200° are shown in Figs. 2.14 and 2.15, where the middle slice of 4 time-phases out of five time-phases was picked up. With time ordering, the motion of rectal gas and stool can be visible in both cases, without image degradation and artifacts caused by the truncation.

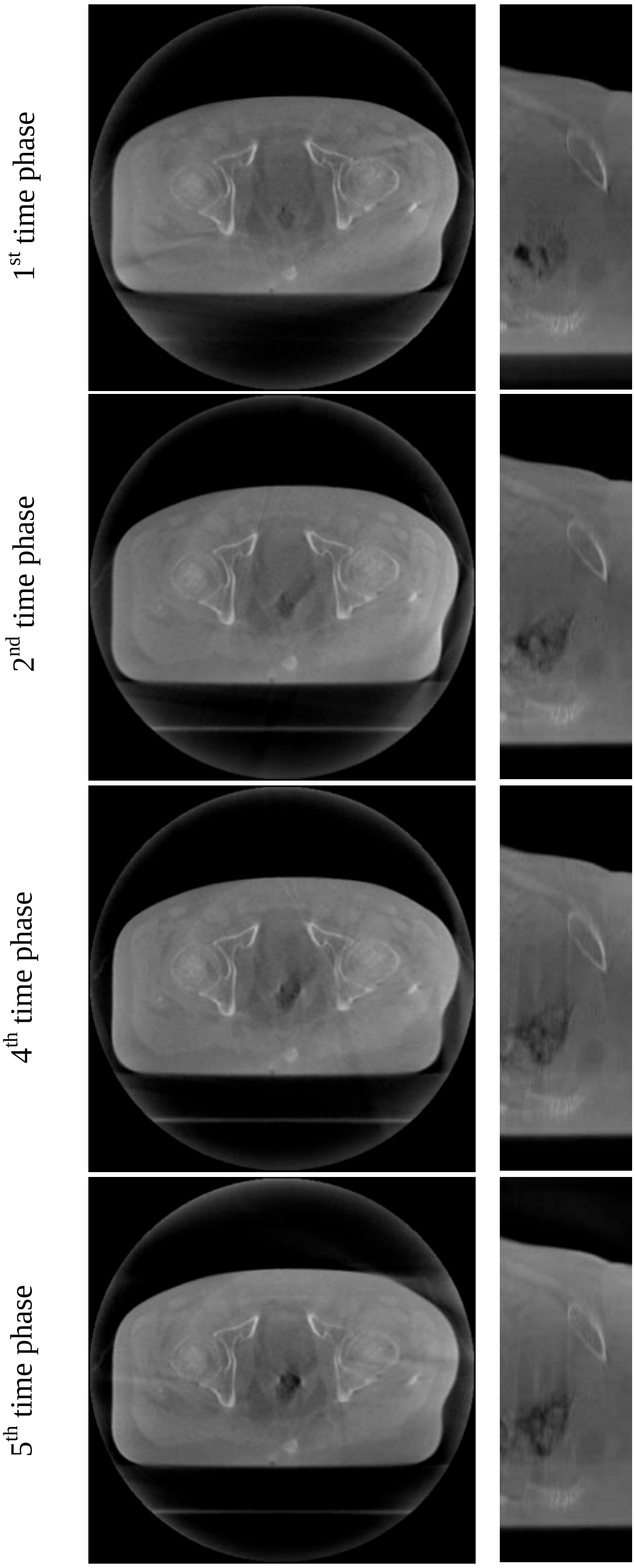

Figure 2.14: Reconstructed axial (left) and sagittal (right) image series of patient A, using time-ordered 4D FDK reconstruction, from 1st to 5th time phase.

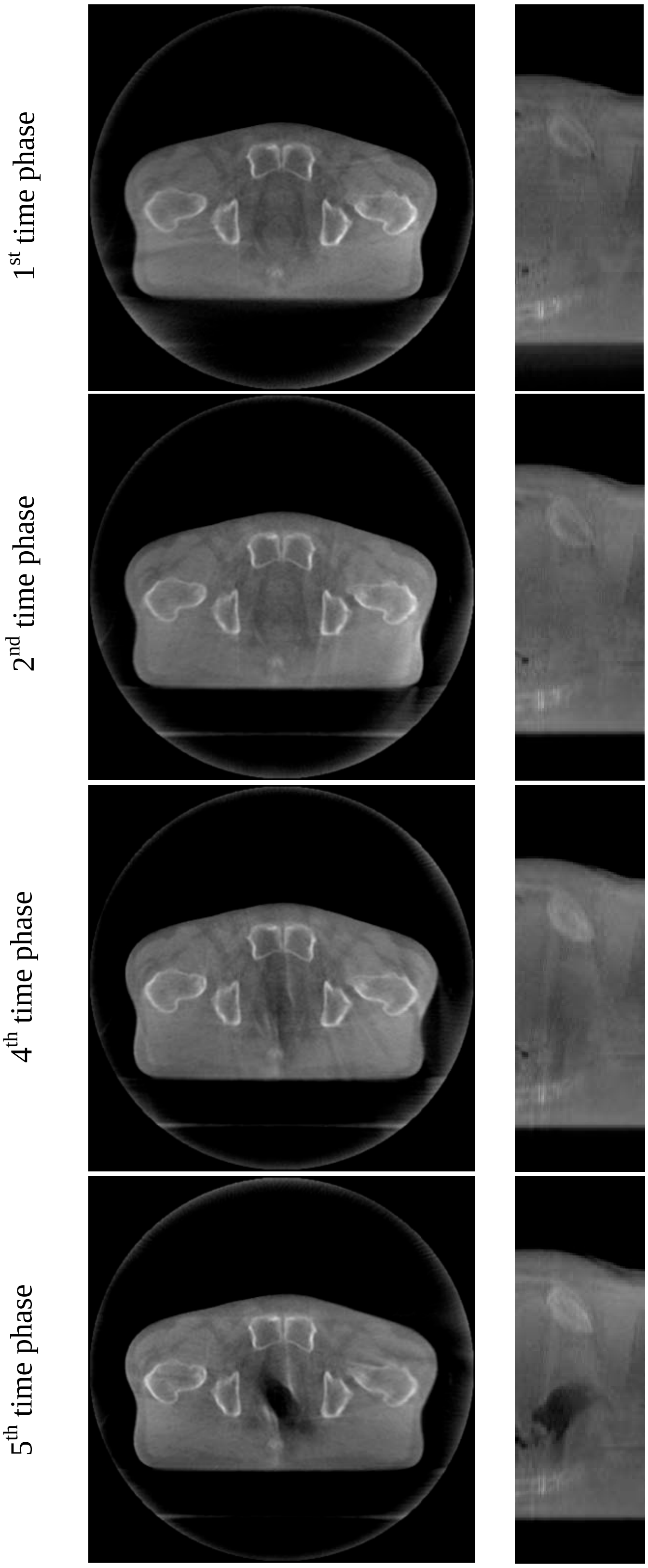

Figure 2.15: Reconstructed axial (left) and sagittal (right) image series of patient B, using time-ordered 4D FDK reconstruction, from 1st to 5th time phase.

2.4. Discussion

A tradeoff between image degradation and temporal resolution can be clearly seen by the results of digital phantom reconstruction. The normalized pixel value profiles along longitudinal axis, shown in Fig. 2.10, indicated that the reconstruction using narrower angular range provides better temporal resolution. The results of the bounding box analysis, on the other hand, indicated the image degradation depending not only on the angular range width, but also on the angle directions used for reconstruction. The reconstruction with narrower angular range gave degradation of object outline, as shown in Fig. 2.11, and the maximum degradation of air sphere estimated by its widths was about 46 % increase in the case of 100° angular range.

It is repeatedly mentioned in this thesis that angular range of 180° plus fan-angle is required for proper reconstruction. Fig. 2.9 demonstrated the degradation of reconstructed image due to insufficient angular range. Following the manner of required angular range, *i.e.* 200° in our system, the best temporal resolution was estimated as 66.7 seconds and 33.3 seconds for gantry rotation time of 120 seconds (patient A) and 60 seconds (patient B), respectively. From the point-of-view of temporal resolution, less angular range might improve its temporal resolution. For example, temporal resolution of 16.7 seconds was provided by projection range of

100° though image degradation of 46 % was occurred. Intrinsically the angular range of projection is directly connected to temporal resolution, especially slowly-rotating CBCT imaging system. That means, the shorter projection range must provide the better temporal resolution. On the other hand, the outline of the patient could not be reconstructed correctly if the better temporal resolution was prioritized, which was demonstrated in Figs. 2.8 and 2.10. This tradeoff is inevitable as long as the FDK method is employed as an image reconstruction method. In order to achieve better temporal resolution, the other reconstruction scheme, iterative reconstruction, will be discussed in the next chapter with less angular range than 180° plus fan-angle cooperating with initial image sets.

Meanwhile, reconstructed images of clinical patients' case demonstrated quite good image quality with projection range of 180° plus fan-angle (=200°), as shown in Figs. 2.14 and 2.15. Those results strongly supported the feasibility of the present idea for the time-ordered image reconstruction. In particular, it should be noted that it was impossible for patient cases to reconstruct the time-ordered motion without projection extension method using mosaicing process.

2.5. Summary of Chapter 2

In Chapter 2, time-ordered 4D reconstruction was introduced by using short-scan FDK method and the reconstructed results has been discussed. The results indicated both advantage and disadvantage of the method. The feasibility of time-ordered image reconstruction was demonstrated while the degradation of images could be caused by too-short projection range for reconstruction of each time-phase. Additionally, it is notable that the proposed projection extension method successfully worked and provided wider projections without non-contiguous boundary. In the next chapter, an iterative reconstruction framework will be introduced for time-ordered 4D reconstruction, combined with projection extension method introduced in this chapter.

3. Time-ordered 4D CBCT reconstruction using MAP iterative reconstruction

3.1. Introduction to Chapter 3

In Chapter 2, time-ordered 4D CBCT reconstruction using short-scan FDK method was introduced and its feasibility and limitation were discussed. To overcome the limitation mentioned in the previous chapter, which is tradeoff between temporal resolution and integrity of reconstructed images, iterative reconstruction approach has been proposed; total-variation based compressed sensing (TVCS) and prior-image constrained compressed sensing (PICCS) have enabled image reconstruction with the limited number of projections and strengthens the reliability of 4D CBCT images[83]–[88].

It has already been introduced by Chen *et al.* (2008) and many other researchers that prior image or prior information helps image reconstruction with limited angular range using iterative reconstruction framework [85]. However, in principle, reconstructed time-ordered image sets should be correlated with not only previously prepared images but also image sets of previous or subsequent time phases in a series of continuous 4D images. This idea urged to develop the reconstruction algorithm considering the constraint from the adjacent time-phase images.

In this study, a series of continuous 4D images is recognized as sequential data and correlated each other, and the new concept, time-ordered chain graph model (TCGM), is introduced in the reconstruction framework.

3.2. Materials and methods

3.2.1. Projection data

The same projection data sets as the study in Chapter 2 were used in this study, an elliptic-cylindrical digital phantom projections containing moving air sphere and two clinical patients' projections of pelvic region. The former one was a set of projections of 512×512 pixels and the latter ones were extended to 512×800 pixels using mosaic process, which was also introduced in Chapter 2.

3.2.2. Framework of MAP iterative reconstruction and its constraint term used in total-variation based compressed sensing (TVCS) and prior-image constrained compressed sensing (PICCS)

In this study, maximum *a posteriori* (MAP) approach was employed as an image reconstruction framework (the detailed description about MAP approach is given in Appendix B). The approach is widely used with specific constraint term, such as TVCS and PICCS. The constraint term characterizes the reconstruction method more specifically. Before introducing TVCS and PICCS, the basic concept of a MAP iterative reconstruction is introduced below.

The MAP iterative reconstruction is based on a method to maximize the logarithmic likelihood function $P(\boldsymbol{\mu}|\boldsymbol{y})$, which is a probability to obtain the reconstructed volume $\boldsymbol{\mu}$, when the projection data set $\boldsymbol{y}$ is given. Assuming the Poisson distribution in the photon detection at the x-ray device, the following equation is derived (and see Appendix B, as well),

$$\boldsymbol{\mu}^* = argmax[-\boldsymbol{n}^T \cdot \boldsymbol{y}^* - \|\boldsymbol{n}^*\|_1 + \lambda R(\boldsymbol{\mu})], \tag{3-1}$$

where $\boldsymbol{n}$ means the observed photon number, which has a relation with the projection $\boldsymbol{y}$ as in the device pixel i, $y_i = \ln n_0/n_i$, where n_0 is the number of photons at the x-ray source. The asterisk in $\boldsymbol{\mu}$, $\boldsymbol{y}$, and $\boldsymbol{n}$ indicates the corresponding expectation value. The term $R(\boldsymbol{\mu}) = \ln P(\boldsymbol{\mu})$ is regarded as the regularization or constraint term, which is related with the prior probability $P(\boldsymbol{\mu})$. λ is the regularization parameter to control the weight of regularization function term for the data fidelity term given by $-\boldsymbol{n}^T \cdot \boldsymbol{y}^* - \|\boldsymbol{n}^*\|_1$ in Eq. (3-1).

The meaning of the term $R(\boldsymbol{\mu})$ is originally the probability of volumetric image $\boldsymbol{\mu}$, but it can be actually considered as the regularization term for image reconstruction. In the context of both TVCS and PICCS, $\boldsymbol{l_1}$-norm of TV-operated image is widely utilized;

$$\|\Psi\boldsymbol{\mu}\|_1 = \sum_{x,y,z}\sqrt{\left(\mu_{x,y,z}-\mu_{x+1,y,z}\right)^2+\left(\mu_{x,y,z}-\mu_{x,y+1,z}\right)^2+\left(\mu_{x,y,z}-\mu_{x,y,z+1}\right)^2+\epsilon}\ , \tag{3-2}$$

where ϵ is a small constant which ensures that the total variation is differentiable at the origin. The TV operator Ψ is known as one of the sparsifying transforms, and its $\boldsymbol{l_1}$-norm is to be minimized in the compressive sense.

In addition to the TV-term, the difference between reconstructed image $\boldsymbol{\mu}$ and prior image $\boldsymbol{\mu}_{prior}$, can be included as prior-image constraint (PIC). Then, $R(\boldsymbol{\mu})$ is expressed as,

$$R(\boldsymbol{\mu}) = \alpha\|\Psi\boldsymbol{\mu}\|_1 + \beta\left\|\Psi\left(\boldsymbol{\mu}-\boldsymbol{\mu}_{prior}\right)\right\|_1 \tag{3-3}$$

where α and β are weights of TV and PIC terms, respectively. In the case of image reconstruction using PICCS, both constraint terms are cooperated, and as a weight, 0.09 and 0.91 were proposed, respectively, by Chen *et al.*[85]

3.2.3. Time-ordered chain graph model (TCGM)

In this study, the issue to be dealt with is non-periodic time-ordered phenomena, such as gastrointestinal peristaltic motion and time progress of contrast agent. The image reconstruction is implemented by dividing several time phases, and then time-ordered volumetric images can be obtained. In this context, it is likely to assume intuitively that the time-adjacent volumetric images do not so much differ from each other. Thus, it would be justified to include the correlation between the time-adjacent volumetric images as the prior information in the reconstruction scheme. In the manner of graphical model [89], a lowest-order correlation is expressed using undirected graphical model shown as Fig. 3.2. In the figure, μ_t represents the image volume of t-th time phase, and y_t represents t-th group of cone-beam projections described through the system matrix A. As shown in Fig. 3.2, the imaging volume μ_t and its projections y_t are the latent variables and the observed data, respectively. When assuming continuous measurement of projections, y_t can be regarded as one projection angle data for each t-th time phase, and regarded as a group of several continuous projection angle data when assuming volumetric image reconstruction.

Figure 3.2 demonstrates the concept of the time-ordered chain graph model, which meaning is that the state of t-th time phase locating between (t-1)-th and (t+1)-th time phase is constrained by the image objects of previous time phase μ_{t-1} and next subsequent time phase μ_{t+1}. In all time phases, the images are renewal in the iteration step, so that the constraints can be also dynamically changed. That is, the converged images of all time phases are obtained concurrently.

A term constrained from TCGM can be included in $R(\boldsymbol{\mu})$;

$$R(\boldsymbol{\mu}) = \alpha\|\Psi\boldsymbol{\mu}\|_1 + \beta\left\|\Psi\left(\boldsymbol{\mu} - \boldsymbol{\mu}_{prior}\right)\right\|_1 + \gamma\|\Delta\boldsymbol{\mu}^T\|_1 \qquad \text{(3-4)}$$

Where $\Delta\boldsymbol{\mu}^T$ represents the TCGM regularization term, which can be represented as a TV form of subtracted image,

$$\Delta\boldsymbol{\mu}^T = \Psi(\boldsymbol{\mu}_t - \boldsymbol{\mu}_{t-1}) + \Psi(\boldsymbol{\mu}_t - \boldsymbol{\mu}_{t+1}) \ , \qquad \text{(3-5)}$$

where the first term in r.h.s. of (3-5) means distribution of spatial difference between previous and current phases, whereas the second term means that between current and subsequent phases.

The parameter set (α, β, γ) in Eq. (3-4) controls the relative weight of the three sparsity-promoting terms in the objective function. For PICCS reconstruction, Chen *et al.* (2008) proposed to set the weights of 0.09 and 0.91 for α and β in Eq. (3-3), respectively [85]. In the aim of comparison between three regularization terms in this thesis, especially to clarify difference of temporal advantages between PICCS and TCGM, in this thesis the weight set (α, β, γ) was chosen as $(1.0, 0.0, 0.0)$, $(0.1, 0.9, 0.0)$ and $(0.1, 0.0, 0.9)$, for TVCS, PICCS and TCGM, respectively.

TVCS is also used to create the initial images in PICCS and TCGM. In addition, TVCS-reconstructed images are used as the prior-image constraint in PICCS.

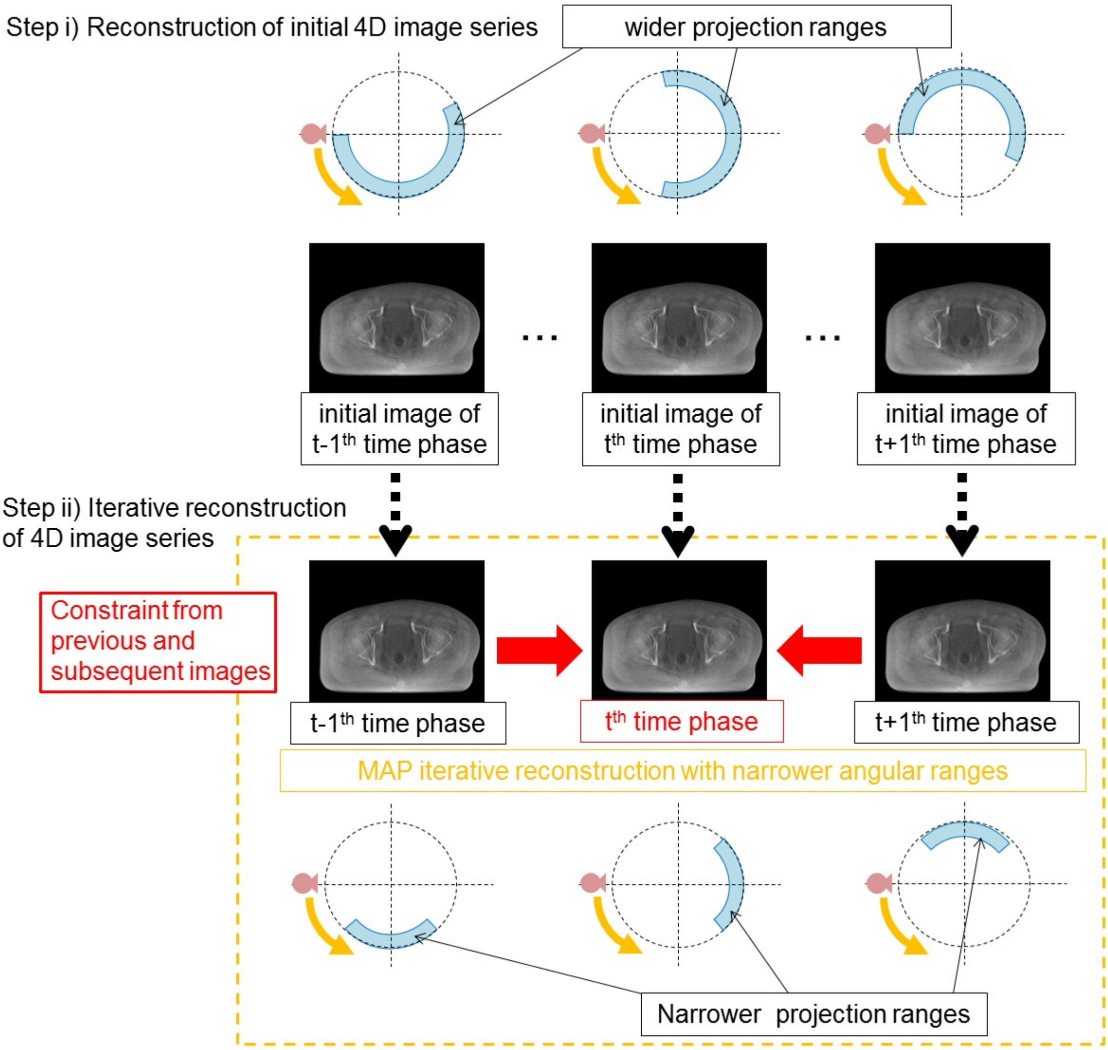

Figure 3.1: Schematic diagram of TCGM reconstruction flow. Initial image series were reconstructed in step i) using wider angular ranges, then iterative reconstruction was implemented in step ii) using narrower ranges.

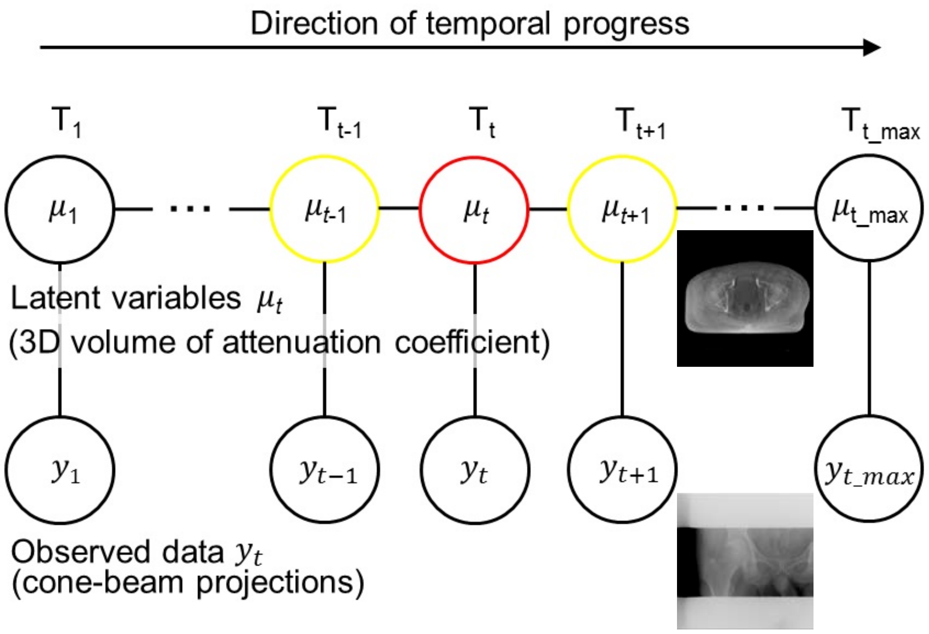

Figure 3.2: The concept of Time-ordered Chain Graph Model.

3.2.4. Reconstruction implementation details and evaluation method of digital phantom

Time-ordered image reconstruction in this chapter was implemented using three different reconstruction methods, TVCS, PICCS and TCGM, introduced in the previous section, for nine time-phases for both digital phantom cases and clinical patients' cases. Angular projection range for reconstruction was 200° for TVCS, and 90° for PICCS and TCGM, and the details of angular projection ranges were mentioned in Table 3.1. It is notable that reconstructed images by TVCS method were used as initial image sets for PICCS and TCGM, and used as prior-image constraint in PICCS as well.

The size of reconstructed digital phantom volume was 256×256 pixels in axial cross-section and 60 slices in longitudinal direction, with 1 mm voxel size. Temporal resolution of reconstructed air sphere contained in the digital phantom was evaluated using penumbral widths along longitudinal axis, which is same direction of motion of air sphere, described as,

$$W_{penumbra} = \frac{W_{10\%} - W_{90\%}}{2}, \tag{3-6}$$

as well as Fig. 3.3.

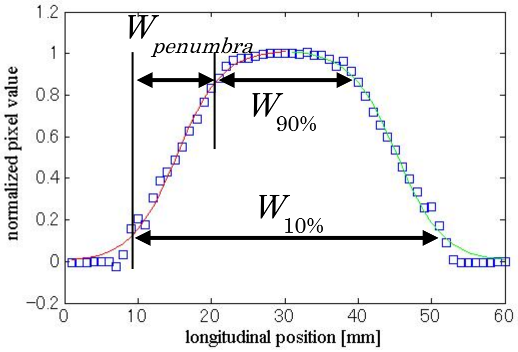

Figure 3.3: An example of normalized pixel value profile and definition of $W_{penumbra}$, $W_{90\%}$, and $W_{10\%}$.

In the case of patients' projection data sets of pelvic region, firstly image mosaicing process using original projections and virtual reprojections were implemented same as in Chapter 2, then the extended mosaic projections were used for image reconstruction using three different reconstruction methods, TVCS, PICCS and TCGM. Details of angular projection ranges were mentioned in Table 3.1., same as digital phantom reconstruction. The reconstruction was implemented for nine time-phases with 400×400 pixels in axial cross-section and 60 slices in longitudinal direction with voxel size of 1 mm.

Table 3.1: The detailed angular range for time-ordered MAP reconstruction

Angular projection range	Number of time-phase	Start angle	End angle	Center angle of projection range
200° for TVCS	1	0°	200°	100°
	2	0°	200°	100°
	3	12.5°	212.5°	112.5°
	4	46.25°	246.25°	146.25°
	5	80°	280°	180°
	6	113.75°	313.75°	213.75°
	7	147.5°	347.5°	247.5°
	8	160°	360°	260°
	9	160°	360°	260°
90° for PICCS and TCGM	1	0°	90°	45°
	2	33.75°	123.75°	78.75°
	3	67.5°	157.5°	112.5°
	4	101.25°	191.25°	146.25°
	5	135°	225°	180°
	6	168.75°	258.75°	213.75°
	7	202.5°	292.5°	247.5°
	8	236.25°	326.25°	281.25°
	9	270°	360°	315°

3.3. Results

3.3.1. Results of digital phantom image reconstruction

Time-ordered images in digital phantom were reconstructed using TVCS (200-degree projection range), PICCS (90-degree projection range), and TCGM (90-degree projection range) as well as the 3D FBP (360-degree projection range). Above three methods provided much less blurring due to the motion, in compared with normal 3D images reconstructed with full projection angles. In addition, PICCS (90-degree projection range) and TCGM (90-degree projection range) provided less blurring images than TVCS (200-degree projection range), mainly due to the narrower projection images used.

Pixel-value profiles of reconstructed volume of 5th time phase out of 9 time phases, along longitudinal axis, were measured and its 10-to-90 % penumbral widths were shown in Table 3.2. The results of PICCS and TCGM were 10.6% and 17.4%, respectively, both of which were narrower than the image volume reconstructed TVCS, 13.2mm. The TCGM yielded the smallest penumbral width, that is, the best temporal resolution.

Table 3.2: Penumbral widths of moving sphere along longitudinal axis.

method	$\mathbf{W_{penumbra}}$
TVCS (360°)	19.9 mm
TVCS (200°)	13.2 mm
PICCS(90°)	11.8 mm
TCGM(90°)	10.9 mm

3.3.2. Results of patients' pelvic image reconstruction

The image reconstruction using TVCS (200-degree projection range), PICCS (90-degree projection range), and TCGM (90-degree projection range) were applied in two clinical patients who underwent cone-beam CT scan in IGRT protocol of the University of Tokyo Hospital. The representative images are presented in Figs 3.4 (axial view), 3.5 (enlarged axial view) and 3.6 (sagittal view) for patient A, and 3.7 (axial view), 3.8 (enlarged axial view) and 3.9 (sagittal view) for patient B, where only 2nd, 4th, 6th, and 8th time phases out of 9 time phases were shown. In both cases, time-ordered motion of rectal gas and flatus could be visible. Especially, the TCGM was the best method to reduce the motion artifact from them.

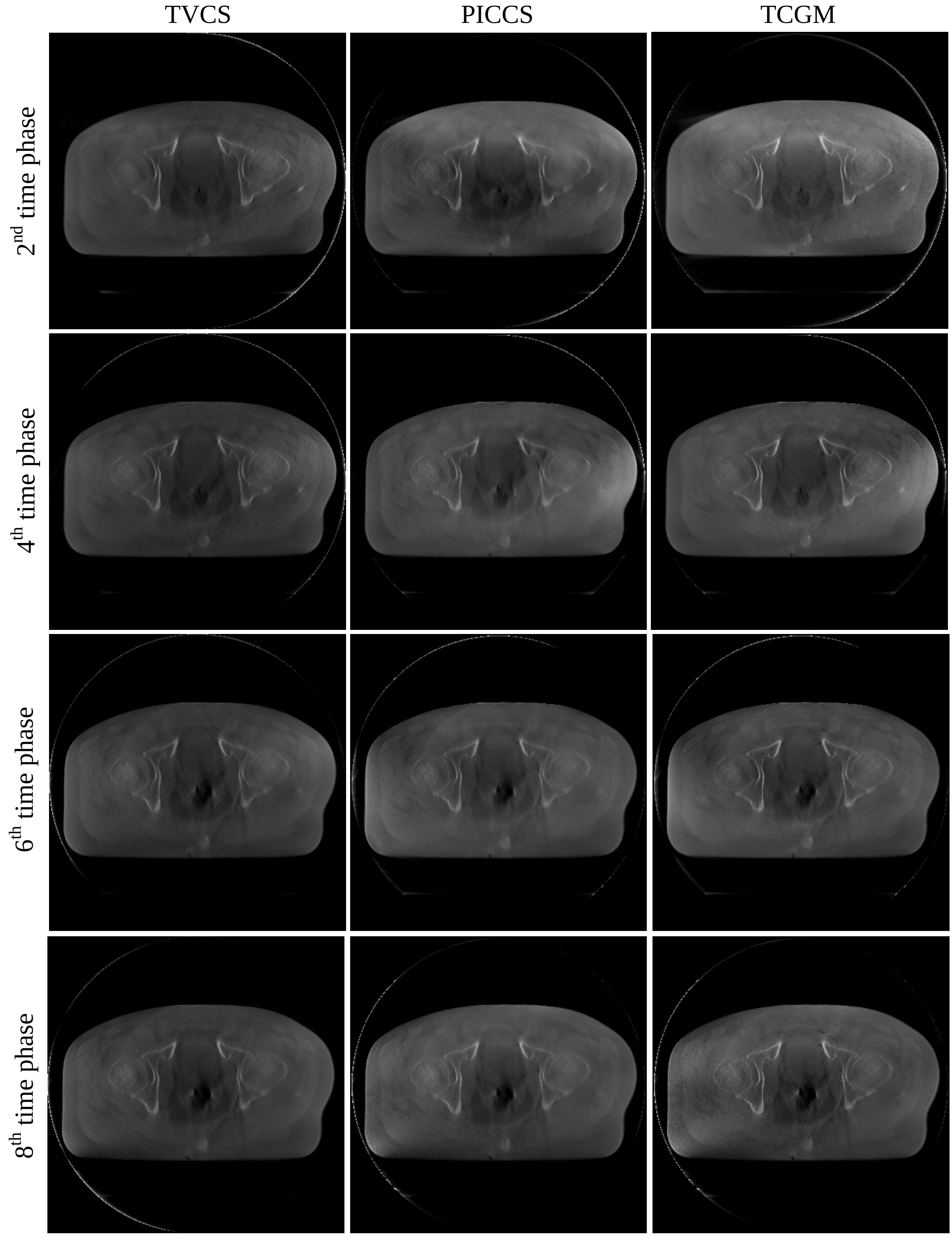

Figure 3.4: Reconstructed axial image series of patient A. Reconstructed images of 2nd, 4th, 6th and 8th time phase out of 9 phases, using TVCS, PICCS and TCGM are in the 1st, 2nd and 3rd columns , respectively.

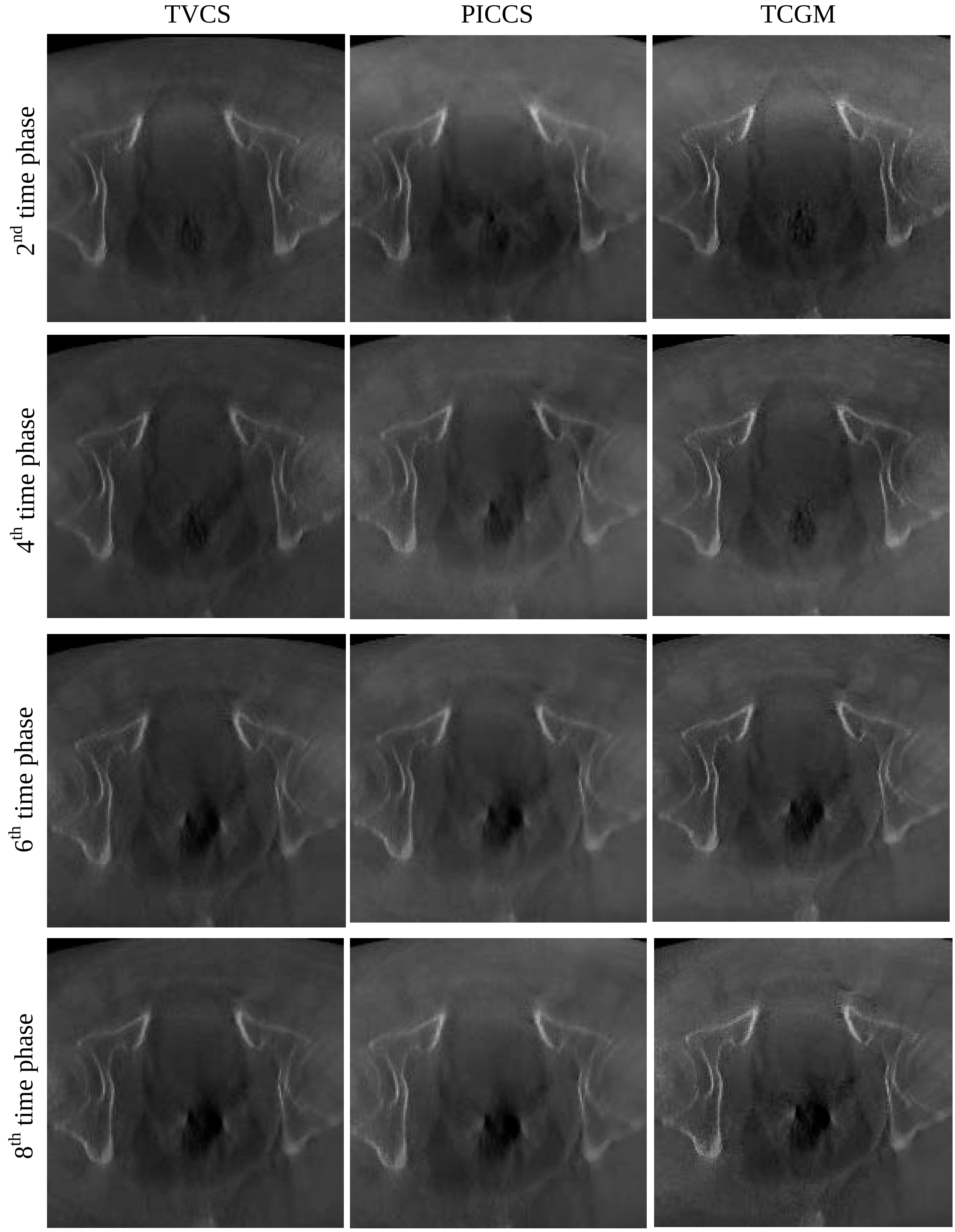

Figure 3.5: Enlarged axial image series of patient A. Reconstructed images of 2nd, 4th, 6th and 8th time phase out of 9 phases, using TVCS, PICCS and TCGM are in the 1st, 2nd and 3rd columns , respectively.

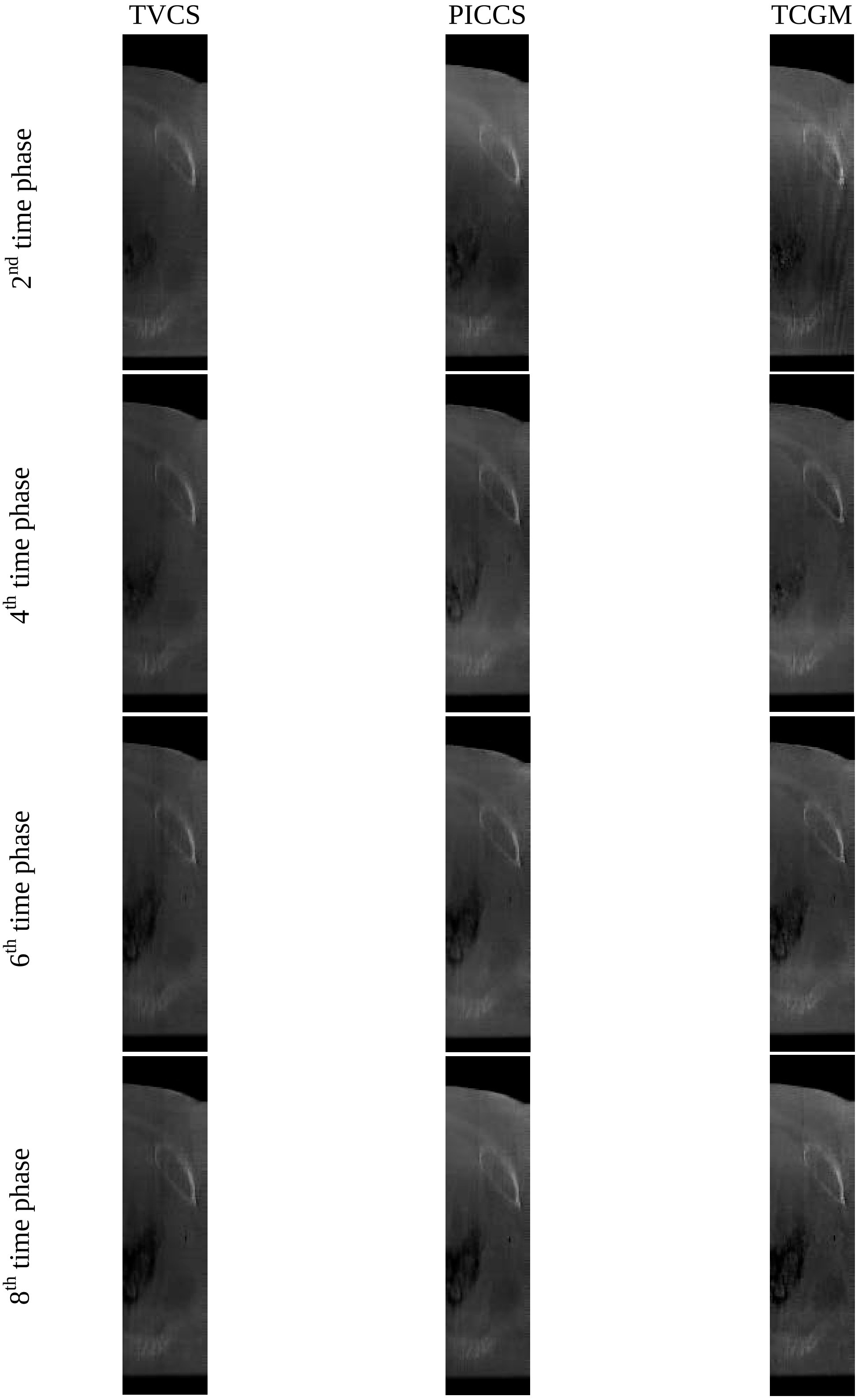

Figure 3.6: Reconstructed sagittal image series of patient A. Reconstructed images of 2nd, 4th, 6th and 8th time phase out of 9 phases, using TVCS, PICCS and TCGM are in the 1st, 2nd and 3rd columns , respectively.

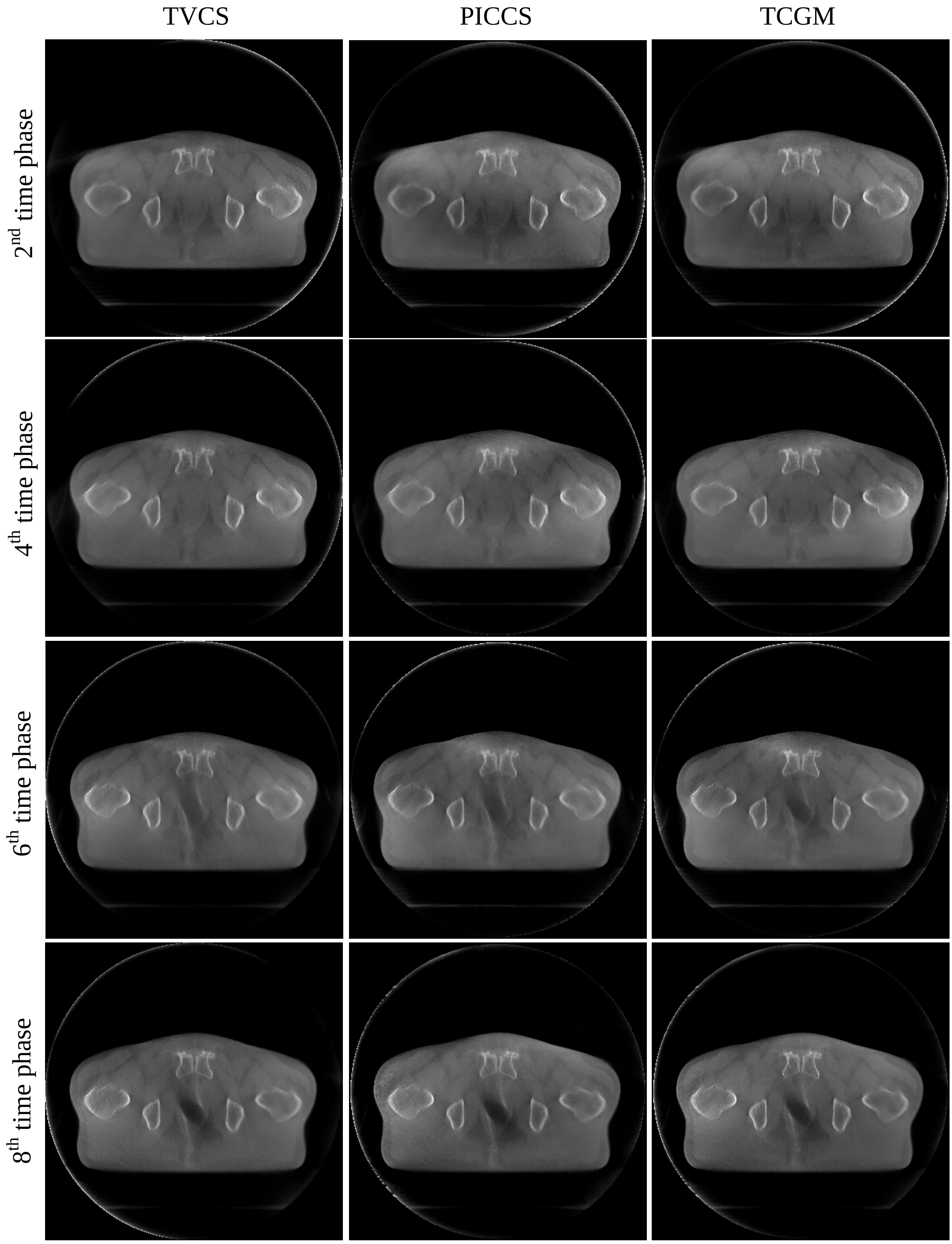

Figure 3.7: Reconstructed axial image series of patient B. Reconstructed images of 2nd, 4th, 6th and 8th time phase out of 9 phases, using TVCS, PICCS and TCGM are in the 1st, 2nd and 3rd columns , respectively.

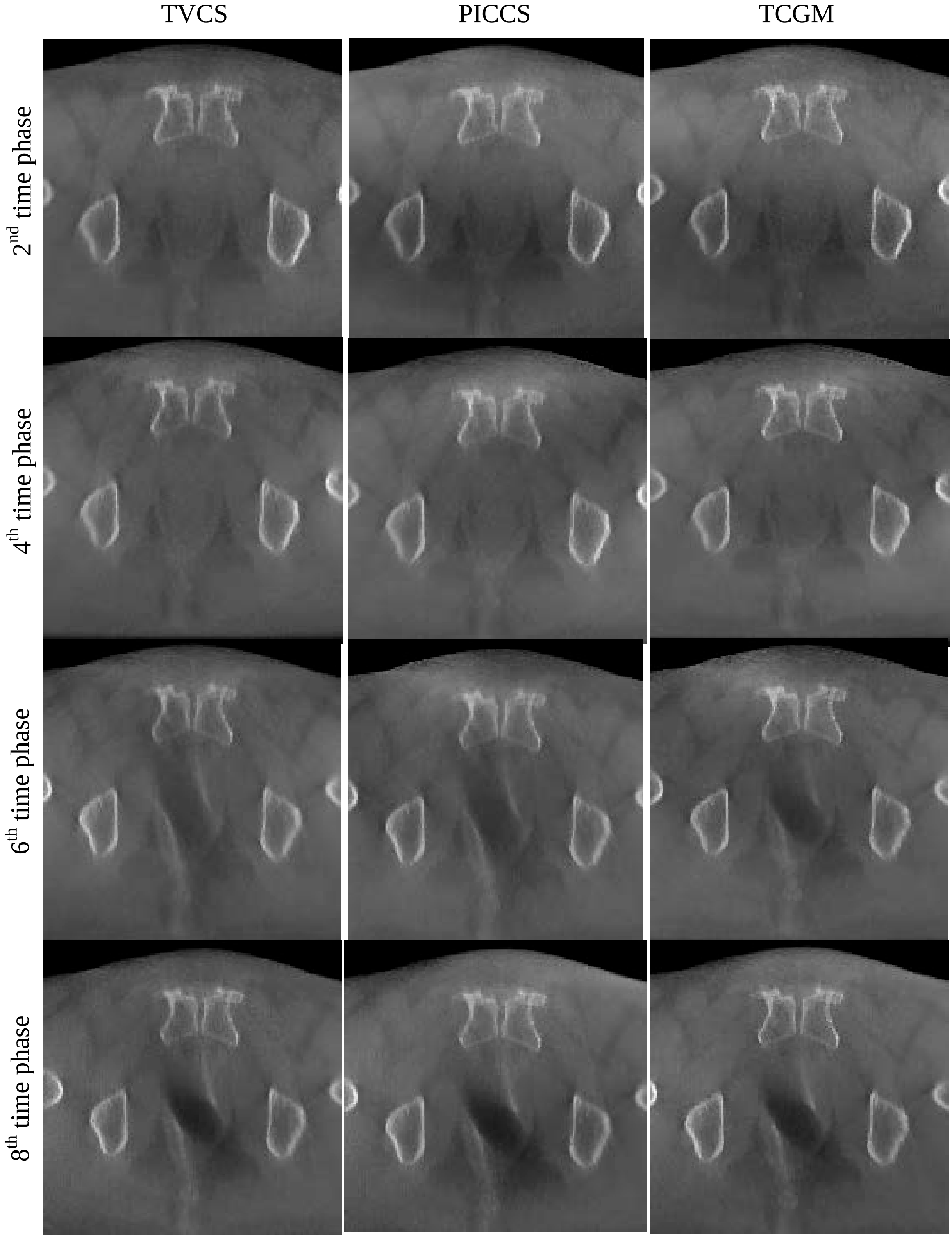

Figure 3.8: Enlarged axial image series of patient B. Reconstructed images of 2nd, 4th, 6th and 8th time phase out of 9 phases, using TVCS, PICCS and TCGM are in the 1st, 2nd and 3rd columns , respectively.

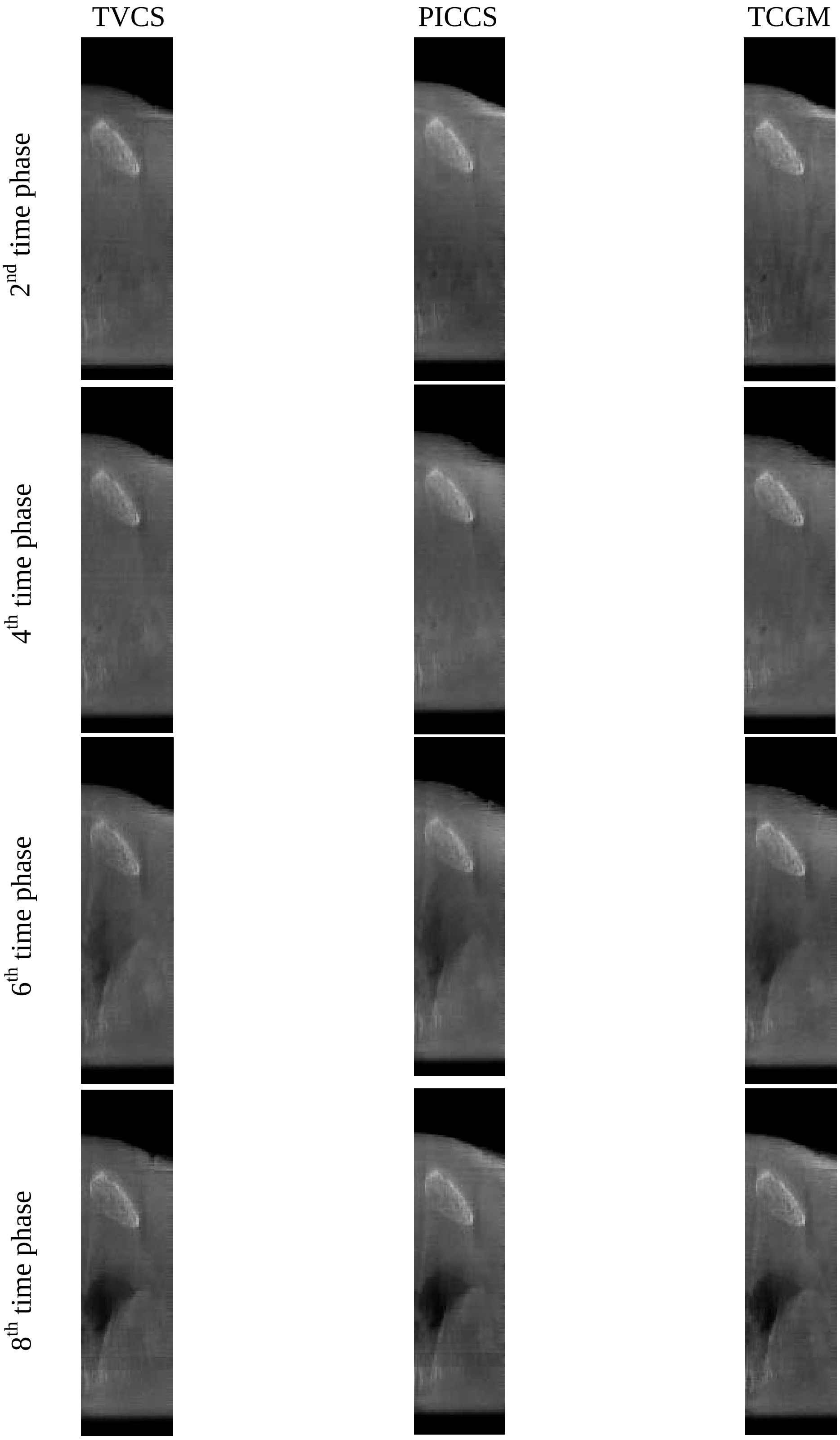

Figure 3.9: Reconstructed sagittal image series of patient B. Reconstructed images of 2nd, 4th, 6th and 8th time phase out of 9 phases, using TVCS, PICCS and TCGM are in the 1st, 2nd and 3rd columns , respectively.

3.4. Discussion

All 4D-CBCT techniques previously proposed in IGRT devices were based on the assumption that the motion of interest objects was periodic, such as the lung motion due to the respiration. With this assumption, the motion signal (e.g. respiratory signal) was used to classify the projection images into several motion-phase bins, so that the volumetric-image series were reconstructed using projection images within each bin. These reconstructed images admittedly included the dimension of time. However, they were still “averaged” 4D images over the gantry rotation and could not represent a non-periodic organ motion, including a base-line shift of the lung-tumor location which is yielded with time progress.

To obtain the time-ordered images, the projection data should be classified by time-ordered phase bins. This idea would work even in the FDK reconstruction algorithm, if the rapid scanning system could be available. In IGRT devices in radiotherapy system, however, the gantry rotation speed is limited by 6.0 degree/s. Therefore, the projection angle range in each time phase has to be as narrow as possible, much less than 180° + fan-angle range, to assure the high time resolution in the reconstructed images. The FDK algorithm could not work now, which requires at least 180° + fan-angle range due to the Shannon-Nyquist sampling theorem. This situation was demonstrated in the previous chapter. A possible approach is to relax this requirement, and the compressed sensing with the prior information is the prime candidate. So far, the FDK reconstruction image with full projection data was used in the prior information. On the other hand, the time-ordered images should be correlated mutually. As in the proposed one, therefore, it is natural to introduce the time-chain model as the prior information.

In this study, the advantage of the TCGM over the TVCS and PICCS was confirmed by the results of the 10-to-90 % penumbral width measurement in the digital phantom; the temporal window width becomes narrower in the PICCS and TCGM, and TCGM was narrower than PICCS. The reason why the TVCS result is the widest is clear, it is simply resulted by the widest projection range of 200 degrees used in this study in comparison with the cases of PICCS and TCGM which were both 90° shown in this study. It is noted that the range less than 200 degrees (= 180° + fan-angle) cannot be applied in the TVCS for the successful image reconstruction. Although in the present study, the time-ordered images were reconstructed by the extended projection image creation even in the TVCS, the TVCS has a disadvantage in the time resolution. On the other hand, the difference between PICCS and TCGM is caused by the difference of prior images used in constraint terms. In the case of

PICCS, iteratively reconstructed image is always compared and constrained with initial image which is reconstructed using TVCS with 200° projection range. Meanwhile TCGM uses images of previous and subsequent images which are being reconstructed in the same iterative process and reconstructed using 90° range of projections. Each 90° range is being overlapped with each other, that means relating projection range is inherently narrower than the one of PICCS.

The time resolution could be improved both in PICCS and TCGM, by increasing the number of time phases and narrowing the corresponding projection range, though there was a trade-off regarding image quality. This study indicated 9-phase results with 90-degree projection range, and the results of clinical patients' pelvic images were really good; they showed rectal gas and flatus moving in rectum. In the case of TCGM, images were reconstructed with less or weaker artifacts from rectal gas, as shown in enlarged axial views. Numerical evaluation of penumbral widths in the digital phantom study was implemented for the case of 3-cm diameter air sphere with 3-cm travel in 1 minute. This moving condition was chosen from an analysis of one patient’s projection set, but it seems relatively slower than the case such as patient B, in which rectal gas was travelling through rectum less than 30 seconds. This situation was not simulated in the chosen condition, but it might be reconstructed appropriately with the reconstruction condition using more time phases and narrower angular range than the reconstruction condition of this study.

The presented TCGM method is inherently possible to provide time-ordered 4D image series with better temporal resolution. The demonstrated results were reconstructed simply using just 90-degree projection range and weights of 0.1 and 0.9 for TV term and TCGM term, and to find optimized parameters must be the future work. The behavior of the present method is quite sensitive to the choice of weights. It might be possible to combine all three methods by choosing non-zero weights for all three weight parameters, for the purpose to provide both better convergence in iterative reconstruction process and better image quality. However, this method can be used to reduce temporal window and to provide image series of non-periodic time-ordered motion, and it should be used to calculate 4D dose distribution.

The remarkable point about the concept of the present method should be noted that the constraint term is based on the series of time-ordered status, which means the *n*-th status locates between *(n+1)*-th and *(n-1)*-th ones and the constraint terms come purely from time-ordered change of statuses. The present method can be improved by incorporating deformation vector field, to demonstrate organ motion and deformation using more essential expression of motion.

3.5. Summary of Chapter 3

In this chapter, the new concept of four-dimensional CBCT reconstruction, based on the Time-ordered Chain Graph Model, has been proposed, and its reconstructed images have been compared to the previous methods based on TVCS and PICCS. Digital phantom results demonstrated that the proposed method can provide 4D image series with the best temporal resolution compared to two other methods. Clinical patients' results showed that the present method is applicable and enable to visualize motion of rectal gas and flatus in rectum.

4. Summary

Throughout the thesis, four-dimensional image reconstruction methods for non-periodic time-ordered anatomical and physiological change have been proposed and discussed. The concept to choose and classify projections for the 4D reconstruction is based on short-scan method, and it is combined with two reconstruction frameworks, FDK reconstruction method and MAP iterative reconstruction method. In the first part of the research, the study using short-scan FDK method demonstrates both its feasibility and the limitation, i.e. shorter projection range improves temporal resolution but it causes degradation of reconstructed object’s outline. The iterative reconstruction using initial image and TCGM constraint term provides the solution to satisfy both temporal resolution and prevention of image degradation.

Back to the motivation of this study, the target of this study is to compute 4D dose distribution on 4D reconstructed CBCT image sets. Although some minor limitations mentioned in Chapter 5 still remain, the author strongly believes that the present study contributes to the initial motivation and implementation of adaptive radiotherapy.

5. Limitation of this research and future work

The proposed method in Chapter 3 enables 4D image reconstruction of CBCT with better temporal resolution, but the thesis is not including oncologists' assessment and comments for the purpose of organ delineation in order to clinical use. Additionally the thesis claimed that the method aims at application for dose calculation in a scenario of adaptive radiotherapy, but the implementation of application is not contained in the thesis. Those two points should be noted as the limitation of this thesis.

The demonstrated results were reconstructed simply using just 90-degree projection range and weights of 0.1 and 0.9 for TV term and TCGM term, and to find optimized weight parameter set must be the future work. It might be possible to combine all three methods by choosing non-zero weights for all three weight parameters, for the purpose to satisfy both better convergence in iterative reconstruction process and better image quality.

One of the drawbacks of TCGM iterative reconstruction method is processing time for image reconstruction. For this problem, as Jia *et al.* mentioned [67], employment of GPU computing might accelerate calculation speed. Image quality of reconstructed images has a room for further improvement, by the implementation of parameter optimization.

For both FDK approach and iterative reconstruction approach, the clinical projection data contain certain amount of scattered photons needed to be corrected, and this issue is related to the general improvement of CBCT imaging. Several researches are already dealing with this scatter correction issue and the solution must be introduced in near future [90]–[92].

The present study also proposed the projection extension method using image mosaicing technique, and the extended area is based on not 4D, but the mixture of 3D and 4D information. In other words, the inner area of the reconstructed volumetric image is 4D but the outer area is a mixture of 3D and 4D. The presented method has a limitation to reconstruct the surface of the patient if the surface moves largely, such as deep breathing and cough during cone-beam projection acquisition.

Acknowledgements

First of all, I would like to express my gratitude for my supervisor Keiichi Nakagawa, head of Radiation Oncology department in The University of Tokyo Hospital, for his inspiring guidance and advice based on his keen instinct throughout this research project. I also would like to express my gratitude for Akihiro Haga, director of Medical Physics Ph.D. course in The University of Tokyo Hospital, for his inspiring guidance, great assistance, and sincere attitude and enthusiasm for physics and mathematics.

I would like to appreciate my co-supervisors, Hideomi Yamashita, Jun’ichi Kotoku in Teikyo University, Yoshitaka Masutani in Hiroshima-City University, Shouhei Hanaoka, Kanabu Nawa, Taiki Magome, Toshikazu Imae, Akira Sakumi, Dousatsu Sakata and Yataro Horikawa, for their kind guidance and assistance. The author also would like to express my appreciation to Kenshiro Shiraishi, Kae Okuma, Wataru Takahashi, Kentaro Yamamoto and all oncologists and radiotherpy technologists in Radiation Oncology department, the University of Tokyo Hospital, for their kind advice and support based on their deep knowledge and experience in Radiation Oncology field.

I would like to acknowledge my respected colleagues and MedPhys friends, Saori Itoh, Satoshi Kida, Naoya Saotome, Masatoshi Hashimoto, Ritu Bhusal Chhatkuli, Daisuke Kon and Shinobu Kumagai, for their advice and encouragement.

I would also like to acknowledge Roel Kierkels, Marianna Sijtsema and Erik Korevaar in University Medical Center Groningen, the Netherlands, Osamu Mitomo in National Hospital Organization Numata Hospital, and Yoshikazu Komuro in Hitachi Ltd.

Finally, I do not know the right word to express my appreciation to my parents for their immense support, thank you.

References

[1] G. Delaney, S. Jacob, C. Featherstone, and M. Barton, "The role of radiotherapy in cancer treatment: Estimating optimal utilization from a review of evidence-based clinical guidelines," *Cancer*, vol. 104, no. 6, pp. 1129–1137, 2005.

[2] International Commission on Radiation Units and Measurements, "Prescribing, recording and reporting photon beam therapy (ICRU report 50)," *ICRU Rep.*, no. November, pp. 357–360, 1993.

[3] International Commission on Radiation Units and Measurements, "ICRU Report 62. Prescribing, Recording, and Reporting Photon Beam Therapy (Supplement to ICRU Report 50)," *J. ICRU*, p. Ix +52, 1999.

[4] M. Van Herk, P. Remeijer, C. Rasch, and J. V. Lebesque, "The probability of correct target dosage: Dose-population histograms for deriving treatment margins in radiotherapy," *Int. J. Radiat. Oncol. Biol. Phys.*, vol. 47, no. 4, pp. 1121–1135, 2000.

[5] M. van Herk, "Errors and margins in radiotherapy.," *Semin. Radiat. Oncol.*, vol. 14, no. 1, pp. 52–64, Jan. 2004.

[6] T. Bortfeld, "IMRT: a review and preview.," *Phys. Med. Biol.*, vol. 51, no. 13, pp. R363–R379, 2006.

[7] S. a Leibel, Z. Fuks, M. J. Zelefsky, S. L. Wolden, K. E. Rosenzweig, K. M. Alektiar, M. a Hunt, E. D. Yorke, L. X. Hong, H. I. Amols, C. M. Burman, A. Jackson, G. S. Mageras, T. LoSasso, L. Happersett, S. V Spirou, C.-S. Chui, and C. C. Ling, "Intensity-modulated radiotherapy," *Z. Med. Phys.*, vol. 8, no. 2, pp. 164–176, 2002.

[8] IMRT Collaborative Working Group, "Intensity-modulated radiotherapy: Current status and issues of interest," *Radiat. Oncol.*, vol. 51, no. 4, pp. 880 – 914, 2001.

[9] S. Webb, "The physical basis of IMRT and inverse planning," *Br. J. Radiol.*, vol. 76, no. 910, pp. 678–689, Oct. 2003.

[10] N. C. Sheets, G. H. Goldin, A. Meyer, T. Stu, J. A. Holmes, B. B. Reeve, P. A. Godley, W. R. Carpenter, and R. C. Chen, "Proton Therapy , or Conformal

Radiation Therapy and Morbidity and Disease Control in Localized Prostate Cancer,” 2012.

[11] J. Boda-Heggemann, F. Lohr, F. Wenz, M. Flentje, and M. Guckenberger, “kV cone-beam CT-based IGRT: a clinical review.,” *Strahlenther. Onkol.*, vol. 187, no. 5, pp. 284–91, May 2011.

[12] M. Chan, J. Yang, Y. Song, C. Burman, P. Chan, and S. Li, “Evaluation of imaging performance of major image guidance systems.,” *Biomed. Imaging Interv. J.*, vol. 7, no. 2, p. e11, Apr. 2011.

[13] M. Kroonwijk, K. L. Pasma, S. Quint, P. C. Koper, a G. Visser, and B. J. Heijmen, “In vivo dosimetry for prostate cancer patients using an electronic portal imaging device (EPID); demonstration of internal organ motion.,” *Radiother. Oncol.*, vol. 49, no. 2, pp. 125–32, Nov. 1998.

[14] V. Mongioj, E. Orlandi, M. Palazzi, E. Deponti, F. Marzia, C. Stucchi, C. Sangalli, C. Fallai, G. Zonca, P. Olmi, and E. Pignoli, “Set-up errors analyses in IMRT treatments for nasopharyngeal carcinoma to evaluate time trends, PTV and PRV margins.,” *Acta Oncol.*, vol. 50, no. 1, pp. 61–71, Jan. 2011.

[15] D. Verellen, M. De Ridder, K. Tournel, M. Duchateau, T. Reynders, T. Gevaert, N. Linthout, and G. Storme, “An overview of volumetric imaging technologies and their quality assurance for IGRT.,” *Acta Oncol.*, vol. 47, no. 7, pp. 1271–8, Jan. 2008.

[16] D. a. Jaffray, J. H. Siewerdsen, J. W. Wong, and A. a. Martinez, “Flat-panel cone-beam computed tomography for image-guided radiation therapy,” *Int. J. Radiat. Oncol. Biol. Phys.*, vol. 53, no. 5, pp. 1337–1349, 2002.

[17] L. a. Dawson and D. a. Jaffray, “Advances in image-guided radiation therapy,” *J. Clin. Oncol.*, vol. 25, no. 8, pp. 938–946, 2007.

[18] D. Létourneau, J. W. Wong, M. Oldham, M. Gulam, L. Watt, D. a. Jaffray, J. H. Siewerdsen, and A. a. Martinez, “Cone-beam-CT guided radiation therapy: Technical implementation,” *Radiother. Oncol.*, vol. 75, no. 3, pp. 279–286, 2005.

[19] M. Birkner, D. Thorwarth, A. Poser, F. Ammazzalorso, and M. Alber, “Analysis of the rigid and deformable component of setup inaccuracies on

portal images in head and neck radiotherapy.," *Phys. Med. Biol.*, vol. 52, no. 18, pp. 5721–33, Sep. 2007.

[20] M. a Hawkins, A. Aitken, V. N. Hansen, H. a McNair, and D. M. Tait, "Set-up errors in radiotherapy for oesophageal cancers--is electronic portal imaging or conebeam more accurate?," *Radiother. Oncol.*, vol. 98, no. 2, pp. 249–54, Feb. 2011.

[21] D. J. Little, L. Dong, L. B. Levy, A. Chandra, and D. a. Kuban, "Use of portal images and BAT ultrasonography to measure setup error and organ motion for prostate IMRT: Implications for treatment margins," *Int. J. Radiat. Oncol. Biol. Phys.*, vol. 56, no. 5, pp. 1218–1224, 2003.

[22] D. Boehmer, P. Maingon, P. Poortmans, R. Miralbell, V. Remouchamps, C. Scrase, A. Bossi, and M. Bolla, "Guidelines for primary radiotherapy of patients with prostate cancer," vol. 79, pp. 259–269, 2006.

[23] K. Shiraishi, M. Futaguchi, A. Haga, A. Sakumi, K. Sasaki, K. Yamamoto, H. Igaki, K. Ohtomo, K. Yoda, and K. Nakagawa, "Validation of Planning Target Volume Margins by Analyzing Intrafractional Localization Errors for 14 Prostate Cancer Patients Based on Three-Dimensional Cross-Correlation between the Prostate Images of Planning CT and Intrafraction Cone-Beam CT during Volumetric Modulated Arc Therapy," vol. 2014, 2014.

[24] K. M. Langen and D. T. Jones, "Organ motion and its management.," *Int. J. Radiat. Oncol. Biol. Phys.*, vol. 50, no. 1, pp. 265–78, May 2001.

[25] H. Onishi, K. Kuriyama, T. Komiyama, K. Marino, M. Araya, R. Saito, S. Aoki, Y. Maehata, L. Tominaga, N. Sano, M. Oguri, K. Onohara, I. Watanabe, T. Koshiishi, K. Ogawa, and T. Araki, "Large prostate motion produced by anal contraction," *Radiother. Oncol.*, vol. 104, pp. 390–394, 2012.

[26] T. Budiharto, P. Slagmolen, K. Haustermans, F. Maes, S. Junius, J. Verstraete, R. Oyen, J. Hermans, and F. Van den Heuvel, "Intrafractional prostate motion during online image guided intensity-modulated radiotherapy for prostate cancer.," *Radiother. Oncol.*, vol. 98, no. 2, pp. 181–6, Feb. 2011.

[27] R. Sripadam, J. Stratford, A. M. Henry, A. Jackson, C. J. Moore, and P. Price, "Rectal motion can reduce CTV coverage and increase rectal dose during prostate radiotherapy: A daily cone-beam CT study," *Radiother. Oncol.*, vol. 90, no. 3, pp. 312–317, 2009.

[28] H. Shirato, Y. Seppenwoolde, K. Kitamura, R. Onimura, and S. Shimizu, “Intrafractional Tumor Motion : Lung and Liver,” vol. 14, no. 1, pp. 10–18, 2004.

[29] K. Nakagawa, A. Haga, S. Kida, Y. Masutani, H. Yamashita, W. Takahashi, A. Sakumi, N. Saotome, T. Shiraki, K. Ohtomo, Y. Iwai, and K. Yoda, “4D registration and 4D verification of lung tumor position for stereotactic volumetric modulated arc therapy using respiratory-correlated cone-beam CT.,” *J. Radiat. Res.*, vol. 54, no. 1, pp. 152–6, Jan. 2013.

[30] J.-J. Sonke, M. Rossi, J. Wolthaus, M. van Herk, E. Damen, and J. Belderbos, “Frameless stereotactic body radiotherapy for lung cancer using four-dimensional cone beam CT guidance.,” *Int. J. Radiat. Oncol. Biol. Phys.*, vol. 74, no. 2, pp. 567–574, 2009.

[31] K. M. Langen, T. R. Willoughby, S. L. Meeks, A. Santhanam, A. Cunningham, L. Levine, and P. a Kupelian, “Observations on real-time prostate gland motion using electromagnetic tracking.,” *Int. J. Radiat. Oncol. Biol. Phys.*, vol. 71, no. 4, pp. 1084–90, Jul. 2008.

[32] P. Kupelian, T. Willoughby, A. Mahadevan, T. Djemil, G. Weinstein, S. Jani, C. Enke, T. Solberg, N. Flores, D. Liu, D. Beyer, and L. Levine, “Multi-institutional clinical experience with the Calypso System in localization and continuous, real-time monitoring of the prostate gland during external radiotherapy.,” *Int. J. Radiat. Oncol. Biol. Phys.*, vol. 67, no. 4, pp. 1088–98, Mar. 2007.

[33] H. Yamashita, K. Okuma, K. Tada, K. Shiraishi, W. Takahashi, S. Shibata-Mobayashi, A. Sakumi, N. Saotome, A. Haga, T. Onoe, K. Ino, M. Akahane, K. Ohtomo, and K. Nakagawa, “Four-dimensional measurement of the displacement of internal fiducial and skin markers during 320-multislice computed tomography scanning of breast cancer.,” *Int. J. Radiat. Oncol. Biol. Phys.*, vol. 84, no. 2, pp. 331–5, Oct. 2012.

[34] J. Mechalakos, E. Yorke, G. S. Mageras, A. Hertanto, A. Jackson, C. Obcemea, K. Rosenzweig, and C. C. Ling, “Dosimetric effect of respiratory motion in external beam radiotherapy of the lung,” vol. 71, pp. 191–200, 2004.

[35] J.-J. Sonke, L. Zijp, P. Remeijer, and M. van Herk, “Respiratory correlated cone beam CT.,” *Med. Phys.*, vol. 32, no. 4, pp. 1176–1186, 2005.

[36] P. T. Lauzier, J. Tang, and G.-H. Chen, “Time-resolved cardiac interventional cone-beam CT reconstruction from fully truncated projections using the prior image constrained compressed sensing (PICCS) algorithm,” *Phys. Med. Biol.*, vol. 57, no. 9, pp. 2461–2476, 2012.

[37] M. J. Zelefsky, H. Chan, M. Hunt, Y. Yamada, A. M. Shippy, and H. Amols, “Long-term outcome of high dose intensity modulated radiation therapy for patients with clinically localized prostate cancer.,” *J. Urol.*, vol. 176, pp. 1415–9, 2006.

[38] R. Kashani, M. Hub, J. M. Balter, M. L. Kessler, L. Dong, L. Zhang, L. Xing, Y. Xie, D. Hawkes, J. a. Schnabel, J. McClelland, S. Joshi, Q. Chen, and W. Lu, “Objective assessment of deformable image registration in radiotherapy: A multi-institution study,” *Med. Phys.*, vol. 35, no. 12, p. 5944, 2008.

[39] B. S. Teh, W. Y. Mai, B. M. Uhl, M. E. Augspurger, W. H. Grant, H. H. Lu, S. Y. Woo, L. S. Carpenter, J. K. Chiu, and E. B. Butler, “Intensity-modulated radiation therapy (IMRT) for prostate cancer with the use of a rectal balloon for prostate immobilization: Acute toxicity and dose-volume analysis,” *Int. J. Radiat. Oncol. Biol. Phys.*, vol. 49, no. 3, pp. 705–712, 2001.

[40] F. Noo, M. Defrise, R. Clackdoyle, and H. Kudo, “Image reconstruction from fan-beam projections on less than a short scan.,” *Phys. Med. Biol.*, vol. 47, no. 14, pp. 2525–2546, 2002.

[41] Y. Liu, H. Liu, Y. Wang, and G. Wang, “Half-scan cone-beam CT fluoroscopy with multiple x-ray sources,” *Med. Phys.*, vol. 28, no. 7, p. 1466, 2001.

[42] D. L. Parker, “Optimal short scan convolution reconstruction for fanbeam CT,” *Med. Phys.*, vol. 9, no. 2, pp. 254–257, 1982.

[43] S. J. Laroque, E. Y. Sidky, and X. Pan, “limited-angle data in diffraction tomography,” vol. 25, no. 7, pp. 1772–1782, 2008.

[44] G. Pang and J. a Rowlands, “Just-in-time tomography (JiTT): a new concept for image-guided radiation therapy.,” *Phys. Med. Biol.*, vol. 50, no. 21, pp. N323–30, Nov. 2005.

[45] D. J. Godfrey, F.-F. Yin, M. Oldham, S. Yoo, and C. Willett, “Digital tomosynthesis with an on-board kilovoltage imaging device.,” *Int. J. Radiat. Oncol. Biol. Phys.*, vol. 65, no. 1, pp. 8–15, May 2006.

[46] D. Yan, F. Vicini, J. Wong, and A. Martinez, “Adaptive radiation therapy,” *Phys. Med. Biol.*, vol. 42, no. 1, pp. 123–132, Jan. 1997.

[47] D. Yan, D. a. Jaffray, and J. W. Wong, “A model to accumulate fractionated dose in a deforming organ,” *Int. J. Radiat. Oncol. Biol. Phys.*, vol. 44, no. 3, pp. 665–675, 1999.

[48] J. Nijkamp, F. J. Pos, T. T. Nuver, R. de Jong, P. Remeijer, J.-J. Sonke, and J. V Lebesque, “Adaptive radiotherapy for prostate cancer using kilovoltage cone-beam computed tomography: first clinical results.,” *Int. J. Radiat. Oncol. Biol. Phys.*, vol. 70, no. 1, pp. 75–82, Jan. 2008.

[49] A. Mencarelli, S. R. van Kranen, O. Hamming-Vrieze, S. van Beek, C. R. Nico Rasch, M. van Herk, and J.-J. Sonke, “Deformable image registration for adaptive radiation therapy of head and neck cancer: accuracy and precision in the presence of tumor changes.,” *Int. J. Radiat. Oncol. Biol. Phys.*, vol. 90, no. 3, pp. 680–7, Nov. 2014.

[50] W. Lu, G. H. Olivera, Q. Chen, K. J. Ruchala, J. Haimerl, S. L. Meeks, K. M. Langen, and P. a Kupelian, “Deformable registration of the planning image (kVCT) and the daily images (MVCT) for adaptive radiation therapy.,” *Phys. Med. Biol.*, vol. 51, no. 17, pp. 4357–74, Sep. 2006.

[51] G. Janssens, J. O. de Xivry, S. Fekkes, A. Dekker, B. Macq, P. Lambin, and W. van Elmpt, “Evaluation of nonrigid registration models for interfraction dose accumulation in radiotherapy.,” *Med. Phys.*, vol. 36, no. 9, pp. 4268–4276, 2009.

[52] A. Vestergaard, L. P. Muren, J. Søndergaard, U. V. Elstrøm, M. Høyer, and J. B. Petersen, “Adaptive plan selection vs. re-optimisation in radiotherapy for bladder cancer: a dose accumulation comparison.,” *Radiother. Oncol.*, vol. 109, no. 3, pp. 457–62, Dec. 2013.

[53] D. L. Schwartz, A. S. Garden, S. J. Shah, G. Chronowski, S. Sejpal, D. I. Rosenthal, Y. Chen, Y. Zhang, L. Zhang, P.-F. Wong, J. a Garcia, K. Kian Ang, and L. Dong, “Adaptive radiotherapy for head and neck

cancer-Dosimetric results from a prospective clinical trial.,” *Radiother. Oncol.*, vol. 106, no. 1, pp. 80–84, 2013.

[54] G. X. Ding, D. M. Duggan, C. W. Coffey, M. Deeley, D. E. Hallahan, A. Cmelak, and A. Malcolm, “Adaptive IMRT A study on adaptive IMRT treatment planning using kV cone-beam CT,” vol. c, pp. 116–125, 2007.

[55] Y. Yang, E. Schreibmann, T. Li, C. Wang, and L. Xing, “Evaluation of on-board kV cone beam CT (CBCT)-based dose calculation.,” *Phys. Med. Biol.*, vol. 52, no. 3, pp. 685–705, 2007.

[56] S. Kida, Y. Masutani, H. Yamashita, T. Imae, T. Matsuura, N. Saotome, K. Ohtomo, K. Nakagawa, and A. Haga, “In-treatment 4D cone-beam CT with image-based respiratory phase recognition.,” *Radiol. Phys. Technol.*, vol. 5, no. 2, pp. 138–47, Jul. 2012.

[57] G. N. Hounsfield, “Computed Medical Imaging,” *J. Comput. Assist. Tomogr.*, vol. 4, no. 5, pp. 665–674, 1980.

[58] T. M. Buzug, *Computed Tomography: From Photon Statistics to Modern Cone-Beam CT*. Springer Science & Business Media, 2008.

[59] T. M. Buzug, “Computed Tomography: From Photon Statistics to Modern Cone-Beam CT (Google eBook),” *Med. Phys.*, vol. 36, no. 8, p. 536, 2008.

[60] J. Hsieh, “Computed Tomography: Principles, Design, Artifacts, and Recent Advances,” in *Computed Tomography, Second Edition: Principles, Design, Artifacts and Recent Advances*, 2003, p. 387.

[61] H. Young, J. Seung-Oh, and P. Jung-Byung, “Fast image reconstruction from fan beam projections using parallel digital signal processors and special purpose processors,” in *TENCON 99. Proceedings of the IEEE Region 10 Conference*, 1999, vol. 2, pp. 1558–1561 vol.2.

[62] L. A. Feldkamp, L. C. Davis, and J. W. Kress, “Practical cone-beam algorithm,” *J. Opt. Soc. Am. A*, vol. 1, no. 6, p. 612, 1984.

[63] S. Webb, “A modified convolution reconstruction technique for divergent beams,” *Phys. Med. Biol.*, vol. 27, no. 3, pp. 419–423, 1982.

[64] E. Y. Sidky, C. Kao, and X. Pan, “Accurate image reconstruction from few-views and limited-angle data in divergent-beam CT,” vol. 14, pp. 119–139, 2006.

[65] J. G. Colsher, “Iterative three-dimensional image reconstruction from tomographic projections,” *Comput. Graph. Image Process.*, vol. 6, no. 6, pp. 513–537, 1977.

[66] M. D. Altschuler, Y. Censor, P. P. Eggermont, G. T. Herman, Y. H. Kuo, R. M. Lewitt, M. McKay, H. K. Tuy, J. K. Udupa, and M. M. Yau, “Demonstration of a software package for the reconstruction of the dynamically changing structure of the human heart from cone beam x-ray projections,” *J. Med. Syst.*, vol. 4, no. 2, pp. 289–304, 1980.

[67] X. Jia, Y. Lou, R. Li, W. Y. Song, and S. B. Jiang, “GPU-based fast cone beam CT reconstruction from undersampled and noisy projection data via total variation,” *Med. Phys.*, vol. 37, no. 4, p. 1757, 2010.

[68] X. Jia, B. Dong, Y. Lou, and S. B. Jiang, “GPU-based iterative cone-beam CT reconstruction using tight frame regularization.,” *Phys. Med. Biol.*, vol. 56, no. 13, pp. 3787–807, Jul. 2011.

[69] G. Pratx and L. Xing, “GPU computing in medical physics: A review,” *Med. Phys.*, vol. 38, no. 5, p. 2685, May 2011.

[70] P. B. Noël, A. M. Walczak, J. Xu, J. J. Corso, K. R. Hoffmann, and S. Schafer, “GPU-based cone beam computed tomography.,” *Comput. Methods Programs Biomed.*, vol. 98, no. 3, pp. 271–7, Jun. 2010.

[71] P. P. Bruyant, “Analytic and Iterative Reconstruction Algorithms in SPECT,” *J. Nucl. Med.*, vol. 43, no. 10, pp. 1343–1358, Oct. 2002.

[72] K. Lange and J. a. Fessler, “Globally convergent algorithms for maximum a posteriori transmission tomography,” *IEEE Trans. Image Process.*, vol. 4, no. 10, pp. 1430–1438, 1995.

[73] P. J. Green, “Bayesian reconstructions from emission tomography data using a modified EM algorithm.,” *IEEE Trans. Med. Imaging*, vol. 9, no. 1, pp. 84–93, 1990.

[74] J. Ma, H. Zhang, Y. Gao, J. Huang, Z. Liang, Q. Feng, and W. Chen, “Iterative image reconstruction for cerebral perfusion CT using a pre-contrast scan induced edge-preserving prior.,” *Phys. Med. Biol.*, vol. 57, no. 22, pp. 7519–42, Nov. 2012.

[75] K. M. Hanson and G. W. Wecksung, “Bayesian approach to limited-angle reconstruction in computed tomography,” *J. Opt. Soc. Am.*, vol. 73, no. 11, p. 1501, Nov. 1983.

[76] J. Luo, W. Li, and Y. Zhu, “Reconstruction from limited-angle projections based on delta - u spectrum analysis,” *IEEE Trans. Image Process.*, vol. 19, no. 1, pp. 131–140, 2010.

[77] D. L. Parker, “Optimal short scan convolution reconstruction for fanbeam CT.,” *Med. Phys.*, vol. 9, no. 2, pp. 254–257, 2011.

[78] J. Lehmann, J. Perks, S. Semon, R. Harse, and A. Purdy, “Commissioning experience with cone-beam computed tomography for image-guided radiation therapy,” vol. 8, no. 3, pp. 21–36, 2007.

[79] R. Szeliski and M. Corporation, “Video Mosaics for Virtual Environments,” vol. 16, no. 2, pp. 22–30, 1996.

[80] Y. Kanazawa and K. Kanatani, “Image mosaicing by stratified matching,” *Image Vis. Comput.*, vol. 22, no. 2, pp. 93–103, Feb. 2004.

[81] A. Ross, S. Shah, and J. Shah, “Image versus feature mosaicing: a case study in fingerprints,” in *SPIE 6202, Biometric Technology for Human Identification III*, 2006, pp. 620208–620208–12.

[82] K. E. Loewke, D. B. Camarillo, W. Piyawattanametha, M. J. Mandella, C. H. Contag, S. Thrun, and J. K. Salisbury, “In vivo micro-image mosaicing.,” *IEEE Trans. Biomed. Eng.*, vol. 58, no. 1, pp. 159–71, Jan. 2011.

[83] D. L. L. Donoho, “Compressed sensing,” *IEEE Trans. Inf. Theory*, vol. 52, no. 4, pp. 1289–1306, 2006.

[84] E. J. Candès, J. Romberg, and T. Tao, “Robust uncertainty principles: Exact signal reconstruction from highly incomplete frequency information,” *IEEE Trans. Inf. Theory*, vol. 52, no. 2, pp. 489–509, 2006.

[85] G.-H. Chen, J. Tang, and S. Leng, “Prior image constrained compressed sensing (PICCS): a method to accurately reconstruct dynamic CT images from highly undersampled projection data sets.,” *Med. Phys.*, vol. 35, no. 2, pp. 660–663, 2008.

[86] S. Leng, J. Tang, J. Zambelli, B. Nett, R. Tolakanahalli, and G.-H. Chen, “High temporal resolution and streak-free four-dimensional cone-beam

computed tomography.," *Phys. Med. Biol.*, vol. 53, no. 20, pp. 5653–5673, 2008.

[87] E. Y. Sidky and X. Pan, "Image reconstruction in circular cone-beam computed tomography by constrained, total-variation minimization.," *Phys. Med. Biol.*, vol. 53, no. 17, pp. 4777–4807, 2008.

[88] E. Y. Sidky, C. Kao, and X. Pan, "Accurate image reconstruction from few-views and limited-angle data in divergent-beam CT," pp. 1–30, 2009.

[89] D. Koller and N. Friedman, *Probabilistic Graphical Models: Principles and Techniques*, vol. 2009, no. 4. 2009.

[90] H. Lee, L. Xing, R. Lee, and B. P. Fahimian, "Scatter correction in cone-beam CT via a half beam blocker technique allowing simultaneous acquisition of scatter and image information.," *Med. Phys.*, vol. 39, no. 5, pp. 2386–95, May 2012.

[91] J. Li, W. Yao, Y. Xiao, and Y. Yu, "Feasibility of improving cone-beam CT number consistency using a scatter correction algorithm.," *J. Appl. Clin. Med. Phys.*, vol. 14, no. 6, p. 4346, Jan. 2013.

[92] R. Ning, X. Tang, and D. Conover, "X-ray scatter correction algorithm for cone beam CT imaging," *Med. Phys.*, vol. 31, no. 5, p. 1195, 2004.

Appendix A: squared-difference minimization in projection image mosaicing process

As discussed in Section 2.2.5. in Chapter 2, image mosaicing technique was applied in projection extension process. Ideally, this mosaic process should work without any correction. Actually, however, the process needs correction of pixel-value intensity for virtually created reprojections to prevent remaining non-contiguous boundary between original projection and "extended" virtual reprojection area.

The basic idea of pixel-value intensity correction is to correct pixel-value intensity on virtual reprojections using linear function, and to minimize sum of pixel-value difference on each real projection and virtual projection in the evaluated area.

$$\begin{aligned} f(a,b) &= \sum_{n=1}^{N} (x_{Real}^{n} - x_{AdjustedVirtual}^{n})^2 \\ &= \sum_{n=1}^{N} (x_{Real}^{n} - (a \cdot x_{Virtual}^{n} + b))^2 , \end{aligned} \tag{A-1}$$

$$\begin{pmatrix} a \\ b \end{pmatrix} = \arg\min \left\{ f(a,b) \right\} , \tag{A-2}$$

where x_{Real}^{n} and $x_{Virtual}^{n}$ are *n*-th pixel values inside four yellow ROIs, shown in Figs 2.8 (a) and (b), for both real projection and virtual reprojection, respectively, and *N* is a total number of evaluated pixels in those ROIs. $x_{AdjustedVirtual}^{n}$ represents pixel values on virtual reprojections after correction, and the correction function is described using linear function with parameters a and b, and those two parameters are defined for each pairs of real and virtual projection.

When the pixel-value difference in the ROIs between original projection and adjusted virtual reprojection is minimized, the derivatives of $f(a,b)$ regarding a and b must be zero. The derivatives are described as follows:

$$\begin{aligned}\frac{\partial}{\partial a}f(a,b) &= -\sum_{n=1}^{N}\{2x_{Virtual}^{n}(x_{Real}^{n}-(a\cdot x_{Virtual}^{n}+b))\}\\ &= -2\sum_{n=1}^{N}(x_{Real}^{n}\cdot x_{Virtual}^{n})+2a\sum_{n=1}^{N}(x_{Virtual}^{n})^{2}+2b\sum_{n=1}^{N}(x_{Virtual}^{n}),\end{aligned} \quad \text{(A-3)}$$

$$\begin{aligned}\frac{\partial}{\partial b}f(a,b) &= -\sum_{n=1}^{N}\{2(x_{Real}^{n}-(a\cdot x_{Virtual}^{n}+b))\}\\ &= -2\sum_{n=1}^{N}(x_{Real}^{n})+2a\sum_{n=1}^{N}(x_{Virtual}^{n})+2bN\ .\end{aligned} \quad \text{(A-4)}$$

Both derivatives should be zero when $f(a,b)$ is minimum, so parameters a and b can be analytically derived as follows:

$$a=\frac{N\sum_{n=1}^{N}\left(x_{Real}^{n}\cdot x_{Virtual}^{n}\right)-\sum_{n=1}^{N}\left(x_{Real}^{n}\right)\cdot\sum_{n=1}^{N}\left(x_{Virtual}^{n}\right)}{1-\left\{\sum_{n=1}^{N}x_{Virtual}^{n}\right\}^{2}}, \quad \text{(A-5)}$$

$$b=\frac{\sum_{n=1}^{N}\left(x_{Real}^{n}\right)}{N}-\frac{\sum_{n=1}^{N}\left(x_{Virtual}^{n}\right)}{N}\cdot\frac{N\sum_{n=1}^{N}\left(x_{Real}^{n}\cdot x_{Virtual}^{n}\right)-\sum_{n=1}^{N}\left(x_{Real}^{n}\right)\cdot\sum_{n=1}^{N}\left(x_{Virtual}^{n}\right)}{1-\left\{\sum_{n=1}^{N}\left(x_{Virtual}^{n}\right)\right\}^{2}}\ .$$

(A-6)

Appendix B: Framework of MAP iterative reconstruction

In Chapter 3, maximum *a posteriori* probability (MAP) iterative reconstruction approach was used in the time-ordered image reconstruction. Namely, the images are reconstructed via an iterative process to maximize *a posteriori* probability function $P(\mu^*|y)$ described as follows,

$$P(\mu^*|y) = \frac{P(y|\mu^*)P(\mu^*)}{P(y)}, \tag{B-1}$$

where $P(y|\mu^*)$ is the probability of observing the projection data set, y, at the given expectation of image, μ^*, having the prior probability $P(\mu^*)$. The observed projection in a detector element in a certain projection angle, y_i, relates to the corresponding photon count n_i as follows,

$$n_i = n_0 e^{-y_i}, \qquad i = 1, 2, \dots, M. \tag{B-2}$$

For expected value, this is expressed as,

$$n_i^* = n_0 e^{-y_i^*}, \qquad i = 1, 2, \dots, M. \tag{B-3}$$

Here, M is the number of total projection elements given by the product of detector pixel and projection angle numbers, and n_0 is the constant photon number generated in the x-ray source. Assuming a monochromatic spectrum in x-ray beam, the relationship between image and projection becomes linear,

$$\boldsymbol{y}^* = \boldsymbol{A}\mu^*, \tag{B-4}$$

where $\boldsymbol{y}^*$ represents the expected projection set and $\boldsymbol{A}$ is a system matrix which consists of the voxel pass lengths corresponding image $\boldsymbol{\mu}^*$. With Eq. (B-3), therefore, the image $\boldsymbol{\mu}^*$ corresponds to the distribution of the attenuation coefficients in the assumed monochromatic x-ray energy. It is also assumed that the number of photons measured at the detector obey a Poisson distribution. Then, the maximization process of the logarithmic of $P(\boldsymbol{\mu}|\boldsymbol{y})$ is same as the implementation of the following,

$$\boldsymbol{\mu}^* = argmax[-\boldsymbol{n}^T \cdot \boldsymbol{y}^* - \|\boldsymbol{n}^*\|_1 + \lambda R(\boldsymbol{\mu})] \qquad \text{(B-5)}$$

where the term $R(\boldsymbol{\mu}) = \ln P(\boldsymbol{\mu})$ is regarded as the regularization or constraint term discussed in Chapter 3.2. λ is the regularization parameter to control the weight of regularization function term for the data fidelity term given by $-\boldsymbol{n}^T \cdot \boldsymbol{y}^* - \|\boldsymbol{n}^*\|_1$.